Inversion of seismic refraction and wide-angle reflection traveltimes for three-dimensional layered crustal structure

N. Rawlinson,[1,]* G. A. Houseman[1,]† and C. D. N. Collins[2]

[1] *Department of Earth Sciences, Monash University, Clayton, Vic 3800, Australia*
[2] *Australian Geological Survey Organisation, Canberra, ACT 2609, Australia*

SUMMARY

We present a method for the determination of crustal structure by simultaneous inversion of seismic refraction and wide-angle reflection traveltimes for 3-D interface geometry and layer velocity. Crustal structure is represented by layers in which velocity varies linearly with depth, separated by smooth interfaces with a cubic B-spline parametrization. Lateral variations in structure are therefore represented by variations in interface depth only. The model parametrization we have chosen means that ray paths consist of piecewise circular arc segments for which analytic expressions of trajectory and traveltime are calculated. The two-point problem of finding the first-arrival ray path and traveltime of a specified phase between a given source and receiver is solved using a shooting technique. A subspace inversion method is used to solve the inverse problem, which is formulated as a non-linear optimization problem in which we seek to minimize an objective function that consists of a data residual term and a regularization term. Before performing the inversion, each data pick must be assigned as a refraction or reflection from a particular layer or interface. Since our method represents structure in terms of interfaces, fewer parameters would generally be used in a reconstruction compared to an equivalent 3-D variable-velocity inversion. The method is well suited to wide-angle surveys that consist of many sources and relatively few receivers (or vice versa), such as marine shot lines used in conjunction with land-based receivers. Data coverage in this kind of survey is often sparse and, especially if near-offset ray paths are unavailable, highly variable. A 3-D synthetic test with an array consisting of eight sources lying within a three-sided square of 79 receivers is described. The test model consists of a three-interface structure that includes a layer pinch-out, and the synthetic data set comprises 987 refraction and 930 reflection travel times contaminated with 75 ms of data noise. Six iterations of an 18-D subspace method demonstrate that the method can produce an accurate reconstruction that satisfies the data from a 1-D starting model. We also find that estimates of *a posteriori* model covariance and resolution obtained from linear theory are useful in analysing solution reliability despite the non-linear nature of the problem. Application of the method to data collected as part of the 1995 TASGO project in Tasmania shows that the method can satisfy 1345 refraction and reflection traveltime picks with a geologically reasonable and robust 254-parameter three-interface model. The inversion results indicate that the Moho beneath NW Tasmania varies in depth from 27 km near the coast to 37 km near central Tasmania, with the major increase in depth occurring across the Arthur Lineament.

Key words: crustal structure, inversion, ray tracing, refraction seismology, Tasmania.

1 INTRODUCTION

Seismic refraction and wide-angle reflection data (hereafter referred to as wide-angle seismic data) have been used extensively to map the Earth's crustal structure in recent times, generally using traveltimes rather than other components of seismic waves such as amplitudes or waveforms. Interpretation methods for this type of data are often based on the principles of tomographic reconstruction. Typically, the procedure involves a forward step of calculating theoretical data values by line integration through a structure defined by a set of model parameters, and

---

*Now at: Research School of Earth Sciences, Australian National University, Canberra ACT 0200, Australia. E-mail: nick@rses.anu.edu.au
†Now at: School of Earth Sciences, University of Leeds, Leeds, LS2 9JT

an inverse step that manipulates these parameter values to improve the fit between theoretical and observed data. In this paper, we apply this inversion method using wide-angle seismic traveltimes.

To date, most wide-angle seismic traveltime tomography has been 2-D and has included inversion for velocity parameters, interface parameters or both, using refraction and/or reflection traveltimes. Lutter *et al.* (1990) inverted refraction traveltimes for velocity, White (1989) inverted refraction traveltimes for interface depth and velocity, Carroll & Beresford (1996) inverted reflection traveltimes for velocity, Lutter & Nowack (1990) inverted reflection traveltimes for interface depth and Bishop *et al.* (1985), Williamson (1990) and Farra & Madriaga (1988) used different approaches to invert reflection traveltimes for velocity and interface depth. Zelt & Smith (1992) used both refraction and reflection traveltimes to constrain velocity and depth parameters. Methods that invert for both velocity and depth parameters can have difficulty in producing well-constrained solutions due to the fact that there may be insufficient information in traveltime data to resolve the difference between velocity variation and depth variation. Wang & Braile (1996) illustrated this point by unsuccessfully attempting to reconstruct a synthetic test model described by velocity and interface depth parameters using only refraction traveltimes. They found that including wide-angle and normal-incidence reflection traveltimes in their inversion dramatically improved the result.

The 3-D wide-angle tomography problem has not been as widely investigated as its 2-D counterpart, mainly due to the increased cost and time required to collect the data and the added complexities at each step of the inversion process. However, it deserves consideration when the assumption of 2-D structure is not valid or when an in-line array of sources and receivers is not possible. 3-D wide-angle inversion methods and applications have been documented by several authors: Hole (1992) and Zelt & Barton (1998) inverted first arrivals for velocity, Hole *et al.* (1992) inverted first arrivals for interface geometry, Riahi *et al.* (1997) inverted wide-angle reflection traveltimes for interface geometry, and Chiu *et al.* (1986) inverted reflection traveltimes for both interface geometry and layer velocity (assumed constant). Inversion for both laterally varying velocity and interface geometry using refraction and wide-angle reflection data was performed by Zelt *et al.* (1996), although they used a layer-stripping approach and did not simultaneously invert refraction and reflection traveltimes. More recently, Zelt *et al.* (1999) simultaneously inverted reflection and refraction data for both laterally varying velocity and multi-interface structure.

In general, the potential for non-uniqueness in 3-D inversions is greater than in 2-D inversions, since the data/model parameter ratio is often lower, and uniform sampling of the subsurface by the data is much more difficult to achieve. For these reasons, Zelt & Zelt (1998) concluded that, unless a dense grid of shots and receivers is used, it is hard to justify a fully 3-D experiment over a network of 2-D profiles, even if 3-D inhomogeneities are present. 3-D structure can be reasonably inferred from multiple in-line profiles, as demonstrated by Zelt (1994), who simultaneously inverted in-line traveltimes for structural and velocity variations beneath intersecting profiles. However, the nature of the survey region and/or logistical restrictions may leave a 3-D survey as the only practicable option. For example, surveys that involve only marine shots and land-based receivers may provide much more information if ray paths cover a range of azimuths.

This paper introduces a method for the determination of 3-D crustal structure from wide-angle seismic traveltimes using the principles of tomographic reconstruction. The method is applied to models consisting of one or more layers overlying a half-space separated by smooth interfaces. Within a layer, velocity varies linearly with depth with no lateral variation, allowing simple ray tracing to be implemented. Each interface is described by a mosaic of bicubic B-spline surface patches that have the property of being C_2 continuous across sutures. Both the velocity parameters and the interface depths are varied in the reconstruction process. Ray paths within layers consist of circular arc segments whose trajectory and traveltime are computed from analytical expressions. The two-point problem of determining the source–receiver ray paths of specific phases is solved using a shooting method, which uses simple geometric considerations to iteratively adjust the ray projection vector at the source so that the emerging ray more accurately targets the receiver. If multiple two-point paths are found for a single phase, the path with minimum traveltime is used in the inversion. The inverse problem requires the adjustment of model parameter values (velocities and layer depths) to minimize an objective function that contains a data residual term and a regularization term. We use a subspace inversion method that requires the solution of a relatively small system of linear equations and naturally deals with different parameter classes. All refraction and reflection data are used in a simultaneous inversion for all model parameters. The seismic tomography problem is inherently non-linear, so the forward and inverse steps are performed iteratively, with new ray paths found at each iteration.

Following the description of the method, we summarize the results of a 3-D synthetic test used to assess its effectiveness. We choose a source–receiver geometry that simulates surveys that rely on marine shots and land-based receivers. Significant lateral variations in interface structure and a layer pinch-out are included in the test model. The sensitivity of the method to data noise is also investigated. Model resolution and *a posteriori* model covariance are then calculated assuming a locally linear relationship between the data and model parameters at the solution point. The aim here is to show how these quantities may be used to assess the quality of the solution for this class of non-linear inverse problem.

Finally, we apply the method to part of the TASGO wide-angle seismic data set, which was recorded in 1995 by an array of 44 single-component analogue and digital recorders distributed throughout Tasmania, with the seismic sources provided by marine shot lines that circumscribed the island (Chudyk *et al.* 1995). In this example, data from an array of eight receivers that recorded seismic energy from three shot lines located just offshore NW Tasmania are used.

2 METHOD

2.1 Model parametrization

In choosing a suitable model parametrization, our criteria included (1) ability to represent geologically realistic structure, (2) satisfying the data using a minimal number of model parameters, (3) ability to generate refraction and reflection arrivals, (4) compatibility with methods used to solve the forward and

inverse steps, and (5) flexibility to allow for non-uniform node spacing (related to point 2). To these ends, the model parametrization that we employ is for a 3-D stratified velocity structure described as follows.

The model structure is defined by a set of p layers (with the bottom layer being a half-space) separated by $p-1$ smooth continuous interfaces. Within a layer, velocity v varies linearly with depth,

$$v(z) = v_0 - kz,\qquad(1)$$

where z is the vertical coordinate (up is positive), $v_0 = v(0)$ and k is the velocity gradient. Each interface is described by a mosaic of uniform bicubic B-spline surface patches in parametric form. Given a set of control vertices $\mathbf{p}_{i,j} = (x_{i,j}, y_{i,j}, z_{i,j})$, where $i = 1, \ldots, m$ and $j = 1, \ldots, n$, the B-spline for the (i, j)th surface patch $(i = 2, \ldots, m-2; j = 2, \ldots, n-2)$ is

$$\boldsymbol{B}_{i,j}(u, v) = \sum_{k=-1}^{2} \sum_{l=-1}^{2} b_k(u) b_l(v) \mathbf{p}_{i+k, j+l},\qquad(2)$$

so that any point on the surface is a function of two independent parameters u $(0 \le u \le 1)$ and v $(0 \le v \le 1)$. The weighting factors $\{b_i\}$ are the uniform cubic B-spline basis functions (see e.g. Bartels *et al.* 1987). The spline formulation of eq. (2) means that the control vertices are not obliged to lie on a regular grid and, by virtue of its parametric form, the surface that is constructed need not be a single-valued function of depth. Other potentially useful properties of the B-spline parametrization are that the control vertices do not necessarily lie on the surface, and that the surface is everywhere continuous in curvature. Undesirable side effects can be produced by forcing piecewise polynomials to pass through nodes (Shalev 1993) and C_2 continuity is beneficial to ray tracing methods that rely on nearby ray trajectories to vary smoothly in order to find a two-point solution.

Eq. (2) defines $(m-3)(n-3)$ surface patches, but we extend the definition of the surface out to nodes with $i = 1, \ldots, m$ and $j = 1, \ldots, n$ by invoking suitable boundary conditions. To do so, we construct a set of perimeter phantom vertices for $i = 0$ and $m+1$ and $j = 0$ and $n+1$ using the condition that the second partial derivative (with respect to the parametric direction across the boundary) is zero at the endpoint of each boundary curve segment (Barsky 1982).

The model parametrization method described above is quite general with respect to interface geometry, but within a layer, velocity is assumed to vary linearly with depth. Not allowing lateral structure within a layer means that a class of geologically realistic models cannot be explored. However, gross lateral variations within a single layer may be represented by the inclusion of additional internal interfaces that subdivide the layer. In practice, the method is sufficient if it can adequately satisfy the data with a geologically plausible structure.

2.2 Ray tracing

Methods for finding source–receiver traveltimes in 3-D laterally varying structures include ray tracing (Julian & Gubbins 1977; Sambridge & Kennett 1990), numerical solution of the eikonal equation (Vidale 1990; Sethian & Popovici 1999) and network/ graph theory (Cheng & House 1996). Wave front tracking

schemes based on the numerical solution of the eikonal equation are probably the most commonly used to solve the forward step of the 3-D wide-angle tomography problem (Hole 1992; Hole *et al.* 1992; Zelt *et al.* 1996; Riahi *et al.* 1997; Zelt & Barton 1998). Advantages of these schemes over ray tracing include computational speed, ability to find solutions in shadow zones and direct computation of first-arrival traveltimes.

We use ray tracing to solve the forward step of the inversion procedure, however. It is well suited to our choice of model parametrization because the ray path in a layer is defined by an analytic expression and each ray is defined by a relatively small number of circular arc segments.

If a continuous velocity medium is described by $v(x, y, z)$, then a ray path connecting two points A and B is one that extremizes the traveltime integral

$$t = \int_A^B \frac{1}{v(x, y, z)}\, ds,\qquad(3)$$

where s is path length. Using the Euler–Lagrange equation from the calculus of variations, the equation of the ray path that extremizes eq. (3) when v is described by eq. (1) is given in parametric form by

$$\mathbf{x} = \frac{v(z_o)}{k}\left[\frac{a_o(c - c_o)}{1 - c_o^2}, \frac{b_o(c - c_o)}{1 - c_o^2}, 1 - \sqrt{\frac{1 - c^2}{1 - c_o^2}}\, \right] + \mathbf{x}_o,\qquad(4)$$

where $\mathbf{x}_o$ is the origin of the ray segment, $[a, b, c]$ is a unit vector tangent to the ray path and $[a_o, b_o, c_o]$ is a unit vector tangent to the ray path at $\mathbf{x}_o$. Eq. (4) is the parametric equation of a circle in terms of the z-component of the unit direction vector c, and is equivalent to the expressions given in Telford *et al.* (1976) that use inclination angle i as the parameter rather than c (cos $i = c$). The ratio a_o/b_o describes the azimuth of the path, which is constant for a ray segment. Any ray path from a source to a receiver in our model will consist of one or more circular arc segments. When k is positive, the ray segment is concave up, and when k is negative, the ray segment is concave down. The traveltime to a point on the current ray segment is given by

$$t = \frac{1}{2k} \ln\left[\left(\frac{1 + c}{1 - c} \right) \left(\frac{1 - c_o}{1 + c_o} \right) \right] + t_o,\qquad(5)$$

where t_o is the traveltime from the source to $\mathbf{x}_o$.

The point of intersection between a ray and a surface can be found if we equate eq. (2) with eq. (4) to form a system of three non-linear equations for the three unknowns u, v and c. We solve this system using a generalized Newton method. The initial guess required by this method is determined by approximating each surface patch with a mosaic of piecewise triangular plates; the point of intersection between a circular path and a plane can be determined analytically.

To determine the new direction of the ray after it intersects the interface, we use Snell's law. At the point of intersection, let $\mathbf{w}_i$, $\mathbf{w}_r$ and $\mathbf{w}_t$ define the unit tangent vectors to the incident ray, refracted/reflected ray and the surface in the plane defined by $\mathbf{w}_i$ and $\mathbf{w}_n$ ($\mathbf{w}_n$ is the unit normal vector to the surface at the point of intersection). Application of Snell's law and the fact that $\mathbf{w}_r$ is a unit vector and must lie in the same plane as $\mathbf{w}_i$

and $\mathbf{w}_t$ yields

$$\left. \begin{array}{c} \dfrac{\mathbf{w}_r \cdot \mathbf{w}_t}{v_r} = \dfrac{\mathbf{w}_i \cdot \mathbf{w}_t}{v_i} \\[2ex] |\mathbf{w}_r| = 1 \\[1ex] (\mathbf{w}_i \times \mathbf{w}_t) \cdot \mathbf{w}_r = 0 \end{array} \right\}, \tag{6}$$

which can be solved analytically for the three components of $\mathbf{w}_r$. The velocity of the ray immediately before and after intersection is denoted by v_i and v_r respectively. Of the two possible solutions to eq. (6), the refracted ray is the one that maximizes $\mathbf{w}_i \cdot \mathbf{w}_r$. We can use eq. (6) to find the change in direction of refracted or reflected ($v_r = v_i$) rays, although in the latter case, since less calculation is required to determine $\mathbf{w}_n$ than $\mathbf{w}_t$, we can instead solve

$$\left. \begin{array}{c} \mathbf{w}_r \cdot \mathbf{w}_n = -\mathbf{w}_i \cdot \mathbf{w}_n \\[1ex] |\mathbf{w}_r| = 1 \\[1ex] (\mathbf{w}_i \times \mathbf{w}_n) \cdot \mathbf{w}_r = 0 \end{array} \right\}, \tag{7}$$

where again the required solution is the one that maximizes $\mathbf{w}_i \cdot \mathbf{w}_r$.

Refracted and reflected rays thus may be traced through the layered models defined in Section 2.1 after defining a source point and an initial trajectory. The ray path is projected to the point where it hits an interface, where it is refracted or reflected and then projected to the next interface. The cycle is repeated until the ray emerges from the model region. The next step is to find the specific ray paths that end at a receiver. This is the so-called two-point problem and is solved here using a four-step shooting method. The first step of the procedure involves shooting out a coarse spread of rays in constant increments of θ (typically $\sim 2°$) and ϕ (typically $\sim 8°$), the inclination and azimuth respectively of a ray at the source (see Fig. 1a). The purpose of this step is to determine the ray projection angles at the source that bound each refraction and reflection phase type. Step 2 of the method involves shooting out a more concentrated spread of rays of each phase type into the regions defined by the previous step. The angular distance in θ and ϕ between projected rays is typically reduced by a factor of four or more from step 1. Step 3 shoots an even more concentrated spread of rays (we usually decrease the increments of θ and ϕ by a factor

of two or three from step 2) into each region bracketed by four adjacent rays (see Fig. 1b) from step 2 that contains one or more receivers. Step 4 is an iterative step that targets each receiver that falls inside a triangle whose vertices are the endpoints of three adjacent rays from step 3 (Fig. 1c). Let $\mathbf{x}_r$ be the position of the receiver being targeted and $\mathbf{x}_p$ be the point where the nearest ray (θ_i, ϕ_i) intersects the receiver plane $z_p = z_r$. Also, let $s_x = x_p - x_r$ and $s_y = y_p - y_r$ (see Fig. 1c). A more accurate estimate (θ_{i+1}, ϕ_{i+1}) of the initial ray parameters is then obtained by solving

$$\begin{bmatrix} \dfrac{\partial s_x}{\partial \theta} & \dfrac{\partial s_x}{\partial \phi} \\[2ex] \dfrac{\partial s_y}{\partial \theta} & \dfrac{\partial s_y}{\partial \phi} \end{bmatrix} \begin{bmatrix} \theta_{i+1} - \theta_i \\[1ex] \phi_{i+1} - \phi_i \end{bmatrix} = \begin{bmatrix} -s_x(\theta_i, \phi_i) \\[1ex] -s_y(\theta_i, \phi_i) \end{bmatrix}. \tag{8}$$

The new ray is then traced from the source and the procedure is repeated with the derivatives re-evaluated at each iteration until the ray strikes the receiver plane within a specified distance from the receiver. We used a tolerance of 50 m for all ray tracing. The partial derivatives in eq. (8) are approximated by an explicit finite difference using the three nearby rays. If a station falls inside more than one triangle then triplication has occurred. A two-point ray is then found in each case and the ray with minimum traveltime is selected.

If a model consists of p layers, we can look for the first arrivals of up to p refraction phases and $p - 1$ reflection phases. Hence, a refraction phase is identified by the deepest layer it samples while a reflection phase is identified by the reflecting interface; multiples are not included in either case. Our iterative method for determining the correct two-point ray is effective partly because we use interfaces that are C_2 continuous. If we used interfaces composed of piecewise planar segments, for example, the discontinuities in gradient between segments would undermine the basic assumption of eq. (8): that θ and ϕ vary smoothly with s_x and s_y.

2.3 Inversion scheme

The aim of the inversion procedure is to minimize the misfit between observed and calculated traveltimes by adjusting the values of the model parameters, subject to regularization constraints. In our case, we have three classes of model parameters
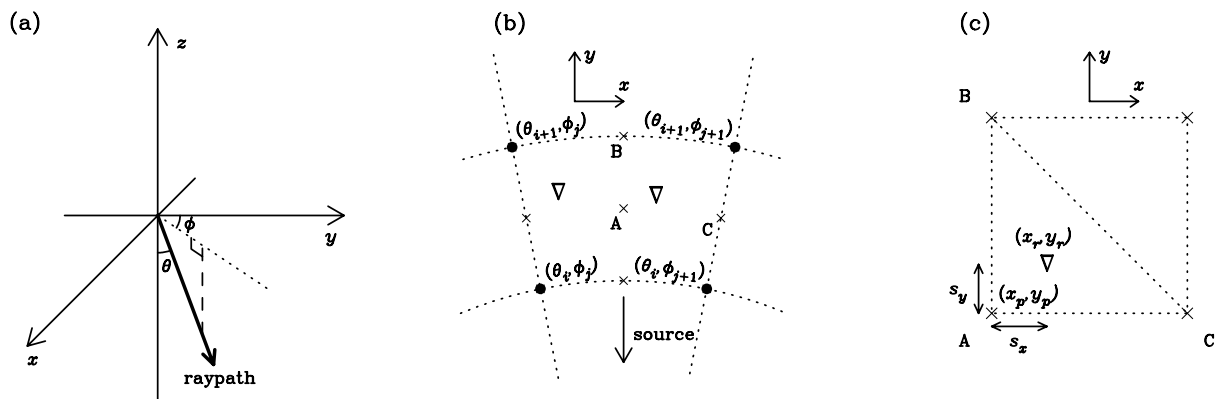

Figure 1. (a) Ray projection parameters at source: θ (inclination) and ϕ (azimuth). (b) If receivers (triangles) fall within a region bracketed by four rays from step 2 (dots) at the surface, a more concentrated shoot (step 3) is used to target the region more closely (crosses). (c) For a receiver lying in the triangle formed by the endpoints of rays A, B and C, the projection parameters of ray A are iteratively adjusted to target the point (x_r, y_r) using position derivatives calculated from the three nearest rays (step 4). See text for full explanation.

that are adjusted: velocities, velocity gradients and the depths of the interface vertices. Let $\mathbf{d}$ denote a data vector of length N that is dependent on a model vector $\mathbf{m}$ of length M as $\mathbf{d} = \mathbf{g}(\mathbf{m})$. If we have an initial estimate $\mathbf{m}_0$ of the model parameters, then comparing $\mathbf{d} = \mathbf{g}(\mathbf{m}_0)$ with the observed traveltimes $\mathbf{d}_{\text{obs}}$ gives an indication of the accuracy of the model. The misfit can be formalized by constructing an objective function $S(\mathbf{m})$ that requires minimization. If we assume the error in the relationship $\mathbf{d}_{\text{obs}} \approx \mathbf{g}(\mathbf{m}_{\text{true}})$ is Gaussian, then a reasonable form for $S(\mathbf{m})$ is

$$S(\mathbf{m}) = (\mathbf{g}(\mathbf{m}) - \mathbf{d}_{\text{obs}})^{\text{T}} \mathbf{C}_{\text{d}}^{-1} (\mathbf{g}(\mathbf{m}) - \mathbf{d}_{\text{obs}})$$
$$+ \varepsilon (\mathbf{m} - \mathbf{m}_0)^{\text{T}} \mathbf{C}_{\text{m}}^{-1} (\mathbf{m} - \mathbf{m}_0), \tag{9}$$

where $\mathbf{C}_{\text{d}}$ is a data covariance matrix, $\mathbf{C}_{\text{m}}$ is an *a priori* model covariance matrix and ε is a damping factor. The damping factor ε governs the trade-off between how well the data are fitted and how near the final model is to the initial model. We do not incorporate a smoothing term into the objective function (e.g. Sambridge 1990) since our interface parametrization is naturally smooth (see eq. 2) and node spacing can be adjusted to suit the resolving power of the data set.

In order to minimize $S(\mathbf{m})$, we use a subspace inversion method. A number of authors (e.g. Kennett *et al.* 1988; Sambridge 1990; Williamson 1990) have described this method so we only provide a brief summary of the technique and show how it applies to our particular problem. The basic assumption of the subspace method, like other gradient-based methods, is that $S(\mathbf{m})$ is sufficiently smooth to validate a locally quadratic approximation about some current model,

$$S(\mathbf{m} + \delta\mathbf{m}) \approx S(\mathbf{m}) + \gamma\delta\mathbf{m} + (\delta\mathbf{m}^{\text{T}} \mathbf{H} \delta\mathbf{m})/2, \tag{10}$$

where $\delta\mathbf{m}$ is a perturbation to the current model and $\gamma = \partial S/\partial\mathbf{m}$ and $\mathbf{H} = \partial^2 S/\partial\mathbf{m}^2$ are the gradient vector and Hessian matrix respectively. Since $\mathbf{g}$ is non-linear, the minimization of $S(\mathbf{m})$ requires an iterative approach,

$$\mathbf{m}_{i+1} = \mathbf{m}_i + \delta\mathbf{m}_i, \qquad i = 0, 1, \ldots, \tag{11}$$

where $\mathbf{m}_0$ is the initial model. The subspace method works by restricting the minimization of the quadratic approximation of $S(\mathbf{m})$ to an n-dimensional subspace of the entire model space, so that the perturbation $\delta\mathbf{m}$ occurs in the space spanned by a set of M-dimensional basis vectors $\{\mathbf{a}^j\}$,

$$\delta\mathbf{m} = \sum_{j=1}^{n} \mu_j \mathbf{a}^j = \mathbf{A}\boldsymbol{\mu}, \tag{12}$$

where $\mathbf{A} = [\mathbf{a}^j]$ is the $M \times n$ projection matrix. The component μ_j determines the length of the corresponding vector $\mathbf{a}^j$ that minimizes the quadratic form of $S(\mathbf{m})$ in the space spanned by $\mathbf{a}^j$. Hence, $\boldsymbol{\mu}$ is found by substituting eq. (12) into eq. (10), differentiating with respect to $\boldsymbol{\mu}$ and setting the left-hand side to zero. The minimum of the quadratic form of $S(\mathbf{m})$ in the n-dimensional subspace is then found when

$$\delta\mathbf{m} = -\mathbf{A}[\mathbf{A}^{\text{T}} \mathbf{H} \mathbf{A}]^{-1} \mathbf{A}^{\text{T}} \gamma. \tag{13}$$

Provided we have γ, $\mathbf{H}$ and the projection matrix $\mathbf{A}$, the evaluation of eq. (13) only requires several matrix multiplications and the solution of a small $n \times n$ system of linear

equations. The gradient vector and the Hessian matrix are

$$\gamma = \mathbf{G}^{\text{T}} \mathbf{C}_{\text{d}}^{-1} [\mathbf{g}(\mathbf{m}) - \mathbf{d}_{\text{obs}}] + \varepsilon\mathbf{C}_{\text{m}}^{-1}(\mathbf{m} - \mathbf{m}_0), \tag{14}$$

$$\mathbf{H} = \mathbf{G}^{\text{T}} \mathbf{C}_{\text{d}}^{-1} \mathbf{G} + \nabla_{\mathbf{m}}\mathbf{G}^{\text{T}} \mathbf{C}_{\text{d}}^{-1} [\mathbf{g}(\mathbf{m}) - \mathbf{d}_{\text{obs}}] + \varepsilon\mathbf{C}_{\text{m}}^{-1}, \tag{15}$$

where $\mathbf{G} = \partial\mathbf{g}/\partial\mathbf{m}$ is the Fréchet matrix of partial derivatives that are calculated during the solution of the forward problem (see Appendix). In our calculations we neglect the second derivative term in $\mathbf{H}$ since its effect is small if $\mathbf{g}(\mathbf{m})$ and $\mathbf{d}_{\text{obs}}$ are not too dissimilar and the forward problem is approximately locally linear.

Our problem has up to three parameter classes: interface depth, velocity and velocity gradient. A strong dependence on scaling and, often, poor convergence (Kennett *et al.* 1988) may be observed when gradient methods such as steepest descent or conjugate gradients are applied to problems with different parameter types. By using a judicious choice of basis vectors, the subspace method can avoid such problems. We construct the $\{\mathbf{a}^j\}$ in terms of the steepest ascent vector in model space $\hat{\gamma} = \mathbf{C}_{\text{m}}\gamma$ at each iteration. Three separate search directions can be obtained by partitioning this vector on the basis of parameter class,

$$\hat{\gamma} = \mathbf{a}^1 + \mathbf{a}^2 + \mathbf{a}^3 = \begin{bmatrix} \hat{\gamma}^1 \\ 0 \\ 0 \end{bmatrix} + \begin{bmatrix} 0 \\ \hat{\gamma}^2 \\ 0 \end{bmatrix} + \begin{bmatrix} 0 \\ 0 \\ \hat{\gamma}^3 \end{bmatrix}, \tag{16}$$

where $\mathbf{a}^1$, $\mathbf{a}^2$ and $\mathbf{a}^3$ represent ascent vectors that lie in the parameter space of interface depth, velocity and velocity gradient respectively. To increase the dimension of the subspace (in order to increase the rate of convergence), we obtain more basis vectors by determining the rate of change of the ascent vectors. A further nine basis vectors are obtained by pre-multiplying $\mathbf{a}^1$, $\mathbf{a}^2$ and $\mathbf{a}^3$ by the model space Hessian $\hat{\mathbf{H}} = \mathbf{C}_{\text{m}}\mathbf{H}$ and partitioning the three vectors that result, as is done in eq. (16). Additional basis vectors can be produced by repeating the process of pre-multiplication of the latest set of vectors by the model space Hessian. Once a suitable number of basis vectors are obtained, they are orthonormalized using Gram–Schmidt orthogonalization. Choosing an appropriate number of basis vectors requires finding an acceptable balance between computational effort and rate of convergence. In the application of our method, we have not used subspaces whose dimensions exceed 18.

The complete inversion method is iterative and, starting from a suitable initial model, each iteration successively uses ray tracing to determine new ray paths, model traveltimes and the Fréchet matrix, and subspace inversion to calculate $\delta\mathbf{m}$. The iterations cease either when the observed traveltimes are satisfied by the model predictions or when the change in $S(\mathbf{m})$ with iteration becomes sufficiently small. If picking errors are constant, then the data are satisfied when the rms difference between observed and model traveltimes falls below the rms picking error. However, since picking errors need not be identical for all picks, the χ^2 misfit, which weights the residuals according to the size of their uncertainties, is used to analyse the data fit. The χ^2 misfit is defined by

$$\chi^2 = \frac{1}{N} \sum_{i=1}^{N} \left(\frac{d_{\text{m}}^i - d_{\text{obs}}^i}{\sigma_{\text{d}}^i} \right)^2, \tag{17}$$

where $\mathbf{g} = \{d_m^i\}$. The quantity $N\chi^2$ is thus equal to the data term of the objective function (eq. 9). The solution fits the data to the level of the noise when $\chi^2 = 1$.

Picked data must be assigned to a reflection or refraction phase from a particular layer or interface prior to the inversion. This may be difficult to do when the velocity contrast across an interface is small, but incorrect assignment may result in that portion of the data being poorly satisfied by the solution model, which suggests either an incorrect assignment or an incorrect pick. Knowing which traveltime is associated with which phase is *a priori* information for the inversion, so if it is possible to identify different phases in the data, then this information should be used to help constrain the solution.

2.4   Estimating variance and damping

We assume uncorrelated errors, and thus define the covariance matrices $\mathbf{C}_d = \{\delta_{ij}(\sigma_d^j)^2\}$ and $\mathbf{C}_m = \{\delta_{ij}(\sigma_m^j)^2\}$. The square root of each non-zero element in $\mathbf{C}_d$ and $\mathbf{C}_m$ thus indicates the estimated uncertainty in the corresponding traveltime and initial model parameter respectively. In a real data inversion, the $\{\sigma_d^j\}$ can be estimated from the picking error of each traveltime. The $\{\sigma_m^j\}$ estimates are based on *a priori* information on the error associated with the initial estimate of each model parameter. If, for example, 1-D refraction interpretations were used to construct the initial model, $\{\sigma_m^j\}$ could be estimated by adjusting the interface and velocity parameters in the refraction interpretation to determine the range over which they will reasonably satisfy the data.

The relative values of σ_d^j control the weight each traveltime datum carries in the inversion. Similarly, the relative values of σ_m^j control the freedom each model parameter has to deviate from its initial value. The choice of $\mathbf{C}_d$ and $\mathbf{C}_m$ also influence the relative magnitudes of the data residual term and the model term in eq. (9), thereby influencing the trade-off in the inversion between satisfying the observed data and matching the initial model estimate. Ultimately, however, this trade-off is controlled by the damping factor ε in the objective function (eq. 9). We require a value of ε that results in a model that satisfies the data well, only differs from the initial model where required by the data, and is physically reasonable. The choice of ε is based on χ^2 misfit versus rms model perturbation (ψ_{mo}) trade-off curves for a range of damping factors, as demonstrated in the synthetic tests (see Section 3). The quantity ψ_{mo} is defined by

$$\psi_{mo} = \sqrt{\frac{\sum_{i=1}^{M} (m^i - m_0^i)^2}{M}} \tag{18}$$

and is calculated separately for each parameter class so that separate trade-off curves are generated for interface depth, velocity and velocity gradient.

2.5   Layer pinch-outs

A layer pinch-out may be represented in the model by two distinct interfaces that are separate in one region of the model but elsewhere come together with an identical set of interface vertices. If a layer pinch-out is expected to occur, then the two interfaces in question are required to have the same vertex distribution in the (x, y) domain. In adjusting the model parameters, we set the condition that no vertex in the upper interface can lie at a greater depth than the corresponding vertex in the lower interface. It follows from the B-spline definition (eq. 2) that the interfaces will not be able to cross over. If, in an inversion, two surface patches become coincident in space, then the ray tracing routine treats them as a single surface patch. Subsequent inversion iterations may separate them or they can be locked together for the remainder of the inversion process if desired.

2.6   Analysis of solution quality

Various methods for evaluating the quality or robustness of a solution to an inverse problem are in use. Parametrizations that describe continuous velocity fields often opt for resolution tests that attempt to reconstruct a synthetic model using the same source–receiver geometry as the real experiment. The so-called 'checkerboard test' is a common example and has been used in local earthquake tomography (e.g. Chiarabba *et al.* 1997), teleseismic tomography (e.g. Steck *et al.* 1998) and wide-angle tomography (e.g. Zelt & Barton 1998). Problems can arise in the apparently straightforward task of translating the synthetic reconstruction results of the checkerboard test into an assessment of solution quality (Lévêque *et al.* 1993), and ray paths through a checkerboard model will differ from those through the solution model if the non-linearity of the problem is accounted for. However, performing a number of these synthetic reconstructions using different structures will improve the reliability of this approach.

Another common approach to analysing solution quality with non-linear inversions is developed from linear theory by assuming that the relationship $\mathbf{d} = \mathbf{g}(\mathbf{m})$ is approximately linear about the solution point. If local linearity applies, then *a posteriori* model covariance $\mathbf{C}_M$ and model resolution $\mathbf{R}$ can be estimated (Tarantola 1987),

$$\mathbf{C}_M \approx \varepsilon[\mathbf{G}^T \mathbf{C}_d^{-1} \mathbf{G} + \varepsilon \mathbf{C}_m^{-1}]^{-1}, \tag{19}$$

$$\mathbf{R} \approx \mathbf{I} - \mathbf{C}_M \mathbf{C}_m^{-1}, \tag{20}$$

where $\mathbf{G}$ is evaluated at the approximate solution. The diagonal elements of $\mathbf{C}_M$ and $\mathbf{R}$ respectively indicate the posterior uncertainty associated with each model parameter and how well each model parameter is independently resolved by the data. Lutter & Nowack (1990), Zelt & Smith (1992) and McCaughey & Singh (1997) have employed these analysis tools in 2-D wide-angle traveltime inversion.

In 3-D velocity inversions, the matrix in eq. (19)— $(\mathbf{G}^T \mathbf{C}_d^{-1} \mathbf{G} + \varepsilon \mathbf{C}_m^{-1})$—may be very large, making calculation of its inverse impractical. Consequently, $\mathbf{C}_M$ and $\mathbf{R}$ are not commonly considered in 3-D problems. The compact parametrization used in our model, however, allows us to economically calculate (using LU decomposition) *a posteriori* model covariance and resolution. We apply this method to the synthetic example in the next section in order to analyse the validity of these robustness estimates, before proceeding to apply the same robustness estimates to a solution derived from real data.

3 SYNTHETIC TESTS

The aim of this section is to examine the performance of our inversion method with 3-D synthetic data by (1) specifying a synthetic (or 'true') model and a source–receiver geometry, (2) generating a synthetic data set by ray tracing through the true model and recording the traveltimes of both refracted and reflected rays, (3) inverting the synthetic data for interface depth and layer velocity starting with a given initial model, and (4) evaluating the differences between the recovered model and the synthetic model. Apart from giving an indication of how well the inversion method can resolve structure, the synthetic tests are also useful for analysing the sensitivity of the method with respect to data noise. In addition, examination of the *a posteriori* model covariance and resolution matrices for the synthetic tests assists us in interpreting those measures for a real data inversion.

The model we use for the synthetic tests consists of three crustal layers overlying a mantle half-space. The three interfaces that define the boundaries between upper crust, middle crust, lower crust and mantle are identically parametrized with 9×9 vertices (see Fig. 2) spaced evenly in both x and y ($\Delta x = \Delta y = 20$ km) with a horizontal coverage of 160×160 km^2. Layer velocities (see Table 1) are chosen to be typical of continental crust. The entire model is defined by 251 parameters comprised of 81 vertical coordinates for each interface and two velocity parameters for each layer. Significant variations in interface depth are present in the model and the lower crustal layer pinches out against the Moho in a large region. The model is depicted in the left-hand column of Fig. 6.

The source–receiver geometry we use for the synthetic tests consists of 79 receivers spaced 5 km apart along three sides of a square, with eight sources lying inside the square. Fig. 2 shows the source–receiver configuration as well as the horizontal positions of the interface vertices. Note that the ratio of sources to receivers we use here is typical of land-based surveys (e.g. Darbyshire *et al.* 1998), but the array geometry is perhaps more likely to be encountered in a marine survey (e.g. the TASGO survey, Chudyk *et al.* 1995), in which case there would be many more sources than receivers. The principle of reciprocity in ray tracing means, however, that we could treat the source array as the receiver array and vice versa without affecting the inversion result.

The synthetic data set was constructed by using the ray tracing method described in Section 2.2 to determine the ray paths of up to four refraction and three reflection phases for each source–receiver pair. The resulting synthetic data set consists of the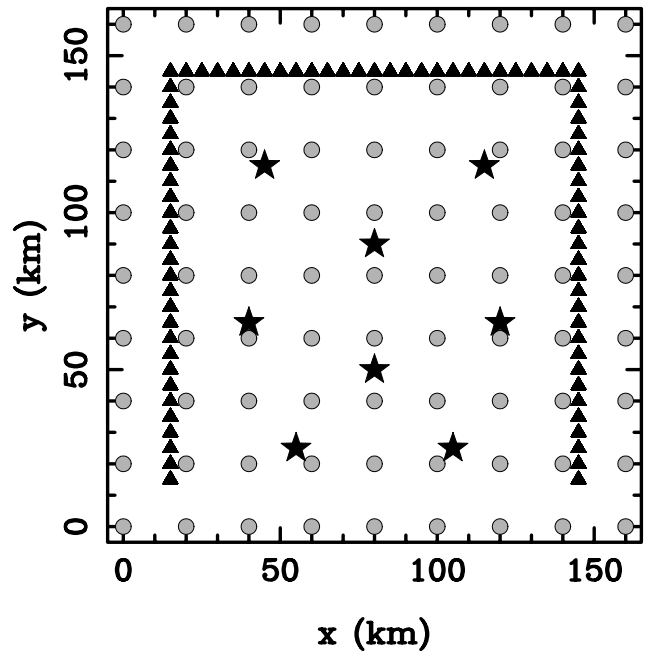 traveltimes of 1917 ray paths (987 refracted and 930 reflected rays). Fig. 3 shows synthetic traveltime curves from the shot at $(x, y) = (55, 25)$ km recorded by the receivers that lie on the line $x = 15$ km. The four refraction phases correspond to rays that turn in the upper, middle, lower crustal and mantle layers. The reflection phases are discernible for all three reflectors. The P_2P and P_mP phases merge at an offset of 90 km as a result of the lower crustal pinch-out. All traveltimes determined by the ray tracing are used in the inversion. In practice, however, the complete offset range of later arrivals determined by ray theory would probably not be picked from real wide-angle data. To simulate the noise content of real data, Gaussian noise with a standard deviation of 75 ms was added to the synthetic traveltimes.

The initial 3-D model estimate from which the inversion commences has a 1-D structure consisting of three planar horizontal interfaces at depths of 7.3, 21.5 and 26.0 km and arbitrary velocity parameters shown in Table 1. A three-interface model is required to account for the four refraction and three reflection curves evident in Fig. 3. Although the

Figure 2. Plan view of the source–receiver array and horizontal positions of interface vertices for the 3-D synthetic model. The locations of the sources and receivers are indicated by stars and triangles respectively. The horizontal positions of the interface vertices (grey dots) are identical for each of the three interfaces.

Table 1. Velocity parameter values of initial, true and recovered models for the synthetic test. The corresponding resolution values associated with the recovered model are also given. Layer 1 is the upper crustal (top) layer and layer 4 is the mantle half-space.

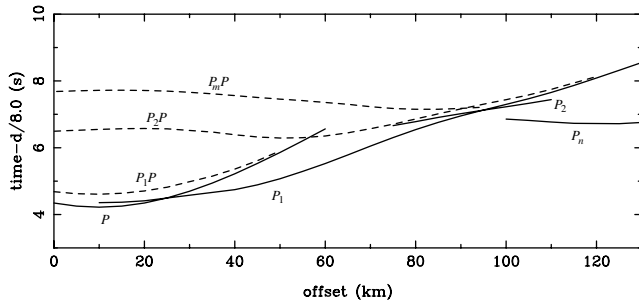| Layer	Initial model		True model		Recovered model		Resolution	
	v_0 (km s^{-1})	k (s^{-1})	v_0 (km s^{-1})	k (s^{-1})	v_0 (km s^{-1})	k (s^{-1})	v_0	k
1	4.60	0.060	4.30	0.050	4.30	0.049	1.00	0.97
2	5.00	0.030	5.20	0.040	5.24	0.038	0.99	0.98
3	6.20	0.040	6.00	0.030	6.13	0.024	0.79	0.76
4	7.20	0.030	7.40	0.020	7.42	0.020	0.74	0.74

Figure 3. Traveltime curves of arrivals from source located at $(x, y) = (55, 25)$ km recorded by receivers that lie along the line $x = 15$ km. Offset is the receiver distance from the start of the line at $(x, y) = (15, 15)$ km, and d is the source–receiver distance. Reflections from the ith interface (P_iP) are denoted by dashed lines, refractions that turn beneath interface i (P_i) by solid lines (P is the direct arrival). Four refraction phases and three reflection phases are evident, indicating the presence of three interfaces.

reflection phases that merge make it tempting to include lateral structure in the starting model, a 1-D starting model is probably a more objective choice if the actual structure is not known *a priori*.

In executing the synthetic data inversion, the dimension of the subspace inversion scheme was set to 18. Of the 18 basis vectors determined, 10 lie in interface depth parameter space, four lie in velocity parameter space and four lie in velocity gradient parameter space. Since there are only four velocity parameters and four velocity gradient parameters, the basis vectors span the model space of both of these parameter classes. We found that this 18-D scheme offered a suitable compromise between the magnitude of the objective function reduction per iteration and the computational effort.

Before commencing the inversion process, we require the values of the damping parameter ε, the data covariance matrix $\mathbf{C}_d$ and the *a priori* model covariance matrix $\mathbf{C}_m$ be specified. The synthetic data were corrupted with Gaussian noise of standard deviation 75 ms, so this value is used in $\mathbf{C}_d : \sigma_d^j = 7.5 \times 10^{-2}$ s, $j = 1, \ldots, N$. In the case of the *a priori* model covariance, the $\{\sigma_m^j\}$ are here based on the rms difference between the true and initial depths of each interface, the true and initial velocities and the true and initial velocity gradients. The values used are 2.0 km for the top interface, 3.0 km for the middle interface, 5.0 km for the bottom interface, 0.23 km s^{-1} for the velocities and 0.01 s^{-1} for the velocity gradient. To determine the most appropriate value of ε, several six-iteration inversions were carried out using values of ε between 0 and 100. Fig. 4(a) shows the reduction in the data residual χ^2 versus rms perturbation of the solution model (relative to the initial model) for six different values of ε for each parameter class. In the range $1.0 \leq \varepsilon \leq 5.0$, the solution is near the minima of the data residual without being highly perturbed from the initial model (Fig. 4a). We also see (Fig. 4b) that this range of damping parameters optimizes the fit of the solution to the true model. Based on this test, we select $\varepsilon = 2.0$ as providing the optimal solution, which we describe below. With real data, the parameter ψ_{mt} is unknown, but this test shows that we can use plots such as Fig. 4(a) to choose a reasonable value for ε.

For $\varepsilon = 2.0$, the χ^2 misfit (eq. 17) decreases monotonically (Fig. 5) from an initial value of 69.12 to 1.02 at iteration six.
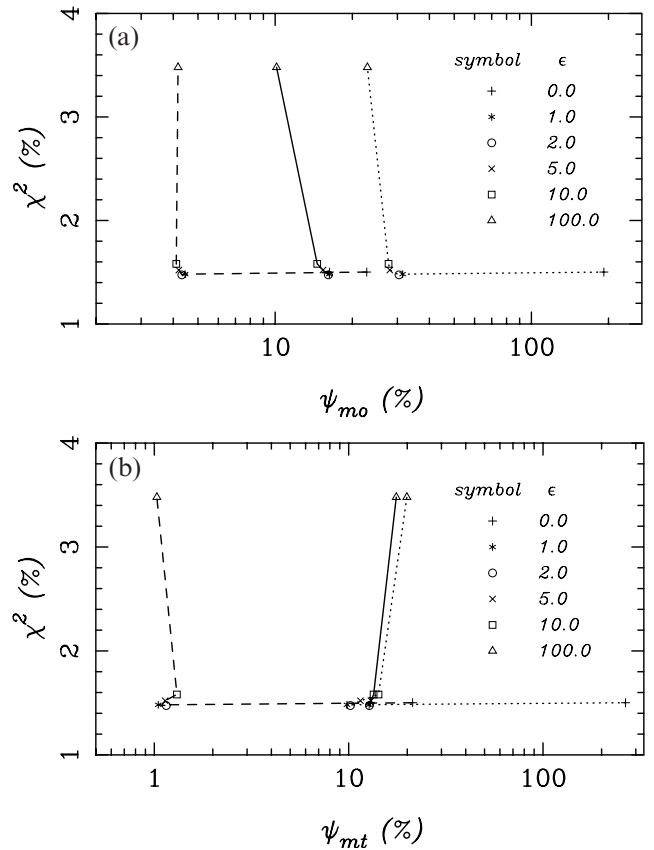

Figure 4. (a) χ^2 data misfit (eq. 17) versus rms model perturbation ψ_{mo} (eq. 18), and (b) χ^2 data misfit versus model inaccuracy ψ_{mt} (obtained from eq. 18 by replacing the initial model $\{m_0^i\}$ with the true model $\{m_t^i\}$), for various values of the damping factor ε after six iterations of the inversion. The three misfit measures χ^2, ψ_{mo} and ψ_{mt} are plotted as a percentage of their initial values (i.e. at iteration zero). The model perturbation ψ_{mo} (and ψ_{mt}) is determined separately for each parameter type: interface node depth (solid line), layer velocity (dashed line) and layer velocity gradient (dotted line).

Correspondingly, the rms traveltime misfit decreases from 624 to 76 ms, a value approximately equal to the standard deviation of the noise added to the data. The improvement in χ^2 misfit between iterations three and six is very small (0.1), and is accompanied by negligible changes in the model parameter values. Such behaviour is indicative of a stable inversion. Fig. 6 shows a comparison between the interface structures of the true model and those of the reconstructed model after six iterations. The basic features of each interface are well recovered except near the edges of the model, where there are no rays and hence no data constraints. Inaccuracies in the recovered model are particularly evident around the edges of interface 3 (Moho), where the initial depths outside the receiver array differ significantly from the true depths. Fig. 7 shows, in four cross-sections at constant x, the starting model, the true model and the reconstructed model. The contrast in accuracy between the reconstruction near the edges of the model and inboard of the receiver array is also evident in these cross-sections.

Velocity parameters are also accurately recovered, as shown by the comparison between the parameters of the true model and those of the reconstructed model in Table 1 and Fig. 8. The average velocity above and below each interface of the
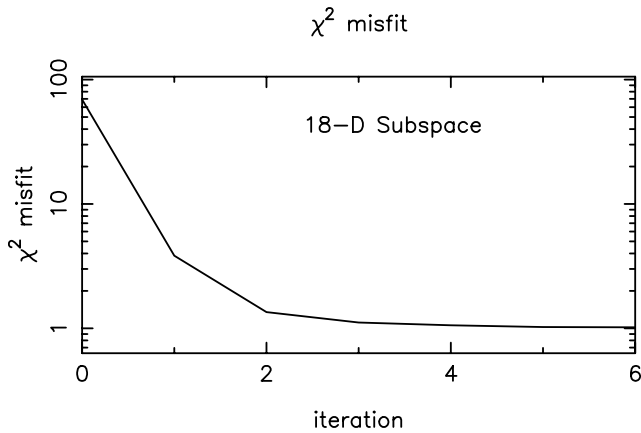
Figure 5. χ^2 data misfit (eq. 17) versus iteration number for 18-D subspace inversion of synthetic traveltime data set with damping parameter $\varepsilon = 2.0$.

true, initial and reconstructed models is shown in Table 2. Even for layer 3, where the two velocity parameters are not particularly well recovered (Table 1), the average velocities at the top and bottom of this layer are quite accurately recovered (Table 2) because the overestimate of v_o is compensated for by the underestimate of k. The relatively low number of rays that turn in layer 3 may account for this trade-off. Table 2 also gives the rms misfit between the true model interface depths and the estimated depths at iteration 0 (initial model) and iteration 6 (final model). Significant improvement is seen in all interfaces, although the final misfit of the bottom interface is significantly larger than those of the top two, mainly due to errors in the unconstrained parts of this interface outside the receiver array.

We now examine how the model resolution matrix **R** (eq. 20) may be used to measure solution quality in this synthetic test. In particular, the diagonal elements of **R** (Fig. 9), which vary between 0 and 1, indicate how well each parameter has been resolved by the data set. Comparison of the resolution matrix entries associated with each interface depth parameter (Fig. 9) and the ray hit diagram (Fig. 10) shows that good resolution of the interface parameters is closely dependent on the proximity of ray–interface hits, particularly of reflections. The most striking feature of Fig. 9 is the contrast between the resolution of the parameters that lie outside the square formed by the receivers and those that lie inside. This contrast is expected because the ray paths do not sample structure that lies outside the array (Fig. 10). The low resolution values and ray hit densities correlate well with those parts of the model that are not accurately reconstructed. For example (see Fig. 6), at $(x, y) = (0, 100+)$ km and

$(x, y) = (160, 100+)$ km, the inversion has failed to pull the bottom interface upwards to pinch out the lower crustal layer. The interface parameters that lie directly adjacent to the receiver lines are consistently better resolved for interface 1 than for the two deeper interfaces because the shallow depth of interface 1 results in a concentration of ray–interface hits close to the sources and receivers (see Fig. 10). It is possible for interface parameters to have non-zero resolution even when they are not in the near vicinity of ray–interface hits, since the spline function that defines each surface patch depends on 16 surrounding nodes (see eq. 2). Although their resolution is not much greater than zero, the nodes of interface 1 that lie outside the receiver array illustrate this effect.

Within the region bounded by the receiver array, the resolution is generally >0.5 for those parts of the interfaces that are accurately reconstructed. Where the reconstruction is less accurate, e.g. at $(x, y) = (80, 80)$ km in interface 2, we generally see a low value for the corresponding resolution matrix entry (0.4 in this case). The resolution matrix entries of the layer velocities and velocity gradients are shown in Table 1. The velocity parameters of the top two layers are well resolved (as expected) because they are quite densely penetrated by rays. The velocity parameters of the third layer are less well resolved, which is explained by the low number of refracted rays that turn in this layer. In general, refracted rays are more important in constraining velocities, while reflected rays are more important in constraining interface depth.

It is common practice with the diagonal elements of the resolution matrix to assign a cut-off value, below which the associated model parameters are considered to be poorly constrained by the data and hence unreliable. For example, Zelt & Smith (1992) used a value of 0.5, while Lutter & Nowack (1990) used a value of 0.6. We performed several synthetic inversions with different array geometries and models and conclude that parameters associated with diagonal elements of the resolution matrix ≥ 0.5 are generally well resolved.

4 APPLICATION TO THE TASGO WIDE-ANGLE DATA SET

During March–April 1995, as part of the TASGO project (Hill & Yeates 1995), a 3-D wide-angle seismic experiment was carried out in Tasmania by the Australian Geological Survey Organisation (AGSO). AGSO's research vessel *Rig Seismic* circumnavigated Tasmania firing $\sim 36\,000$ air-gun shots with an average shot spacing of 50 m. A network of 44 vertical-component analogue and digital recorders distributed throughout Tasmania recorded seismic energy from the shots.

Table 2. Average velocities (in km s^{-1}) immediately above (v_A^a) and below (v_A^b) the initial, true and recovered model interfaces for the synthetic test. The final two columns show the rms misfit between the true model interface depths and estimated model interface depths at iteration 0 (initial model) and iteration 6 (recovered model).

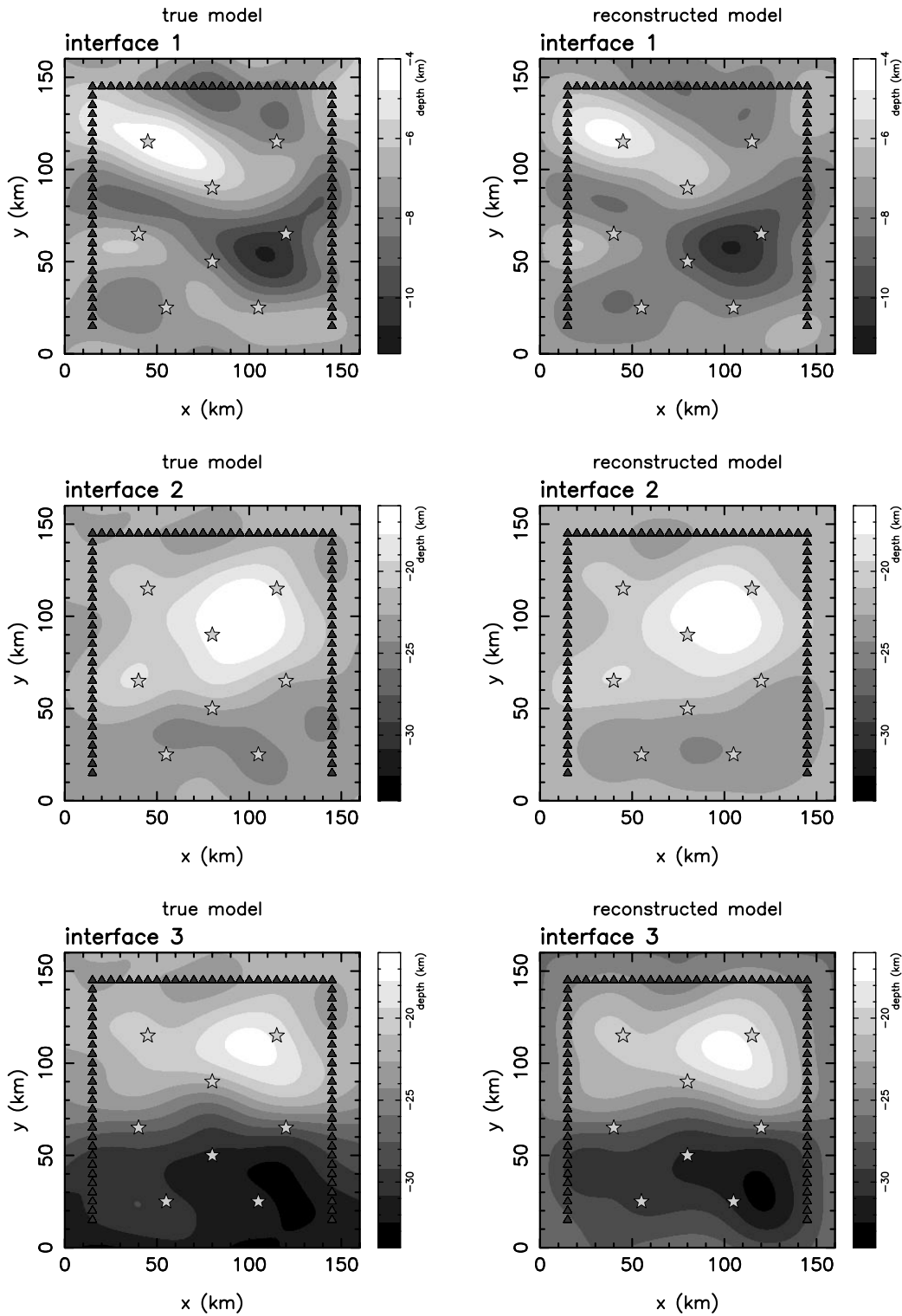| Interface	Initial model		True model		Recovered model		Rms misfit (km)	
	v_A^a	v_A^b	v_A^a	v_A^b	v_A^a	v_A^b	its=0	its=6
1	5.04	5.22	4.67	5.49	4.68	5.53	1.17	0.48
2	5.65	7.06	6.07	6.65	6.05	6.65	2.04	0.69
3	7.24	7.98	6.77	7.91	6.75	7.92	4.63	1.96

Figure 6. Comparison between true model interface depth (left column) and inverted model interface depth (right column) after six iterations of the inversion with $\varepsilon = 2.0$. Interfaces 2 and 3 are given the same greyscale to help identify the pinched-out regions. Figs 6 and 15(a) may be viewed in colour in the online version of the journal (www.blackwell-synergy.com).

Our aim here is to invert a subset of the TASGO wide-angle data set from NW Tasmania to demonstrate the effectiveness of the method applied to real data. The preliminary model of NW Tasmania presented here is the first published 3-D inversion of data from the TASGO wide-angle survey, but we emphasize that it is not the role of this paper to provide

extensive analysis of data or interpretation of results. Instead, we limit our discussion to those aspects of the inversion that illustrate the effectiveness of the new method described above. A detailed examination of the survey operation, data reduction and picking, and interpretation of results using data from all of Tasmania is the subject of a future paper.
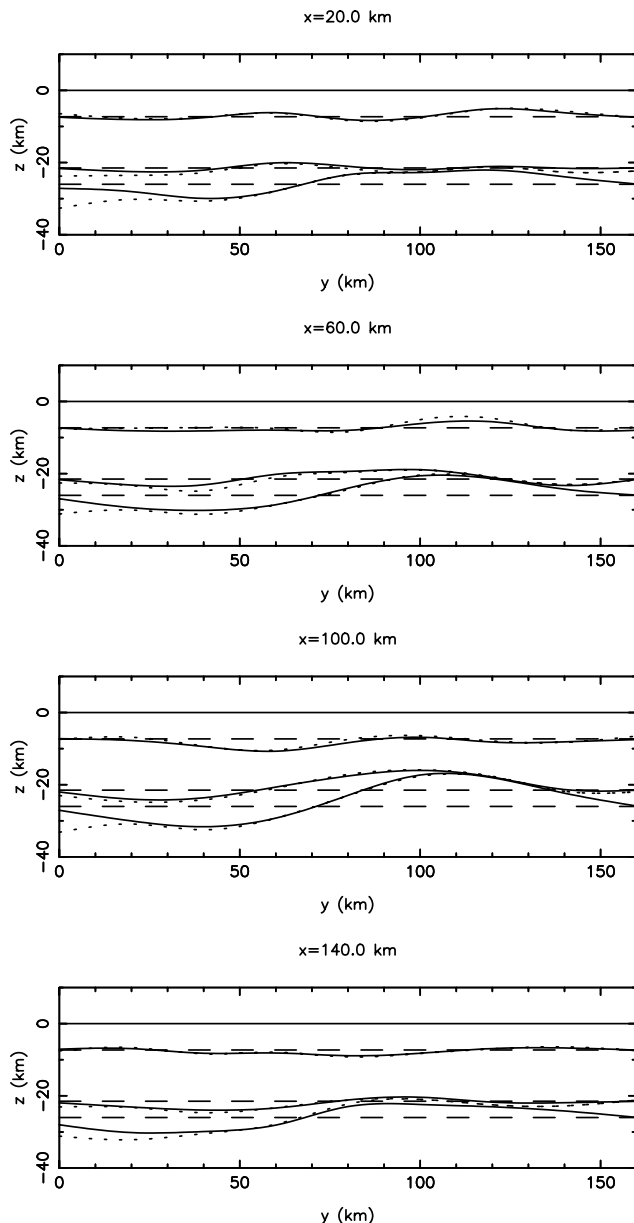
Figure 7. Four cross-sections at constant *x* through the initial model (dashed lines), true model (dotted lines) and reconstructed model (solid lines) after six iterations with $\varepsilon = 2.0$.

Figure 8. Velocity versus depth at two locations in the initial model (dashed lines), true model (dotted lines) and reconstructed model (solid lines). Due to the layer pinch-out, the profile at $(x, y) = (100, 120)$ km essentially shows a two-interface structure, while the profile at $(x, y) = (110, 30)$ km shows a three-interface structure.

In this paper, we analyse a data set that consists of three marine shot lines and eight land-based receivers located in NW Tasmania (see Fig. 11). Equipment problems and the nature of the survey region (Chudyk *et al.* 1995) resulted in not all source-line to receiver combinations providing good data. Where possible, however, phases are picked every 2 km along the lines, resulting in a total of 661 refraction and 684 reflection traveltimes to be inverted for crustal structure. A picking error was associated with each identified arrival based on the clarity of the onset. The rms picking error of all the traveltimes used in the inversion is 115 ms, with the smallest error (50 ms) associated with a near-offset first break and the largest error (210 ms) associated with a Moho reflection.

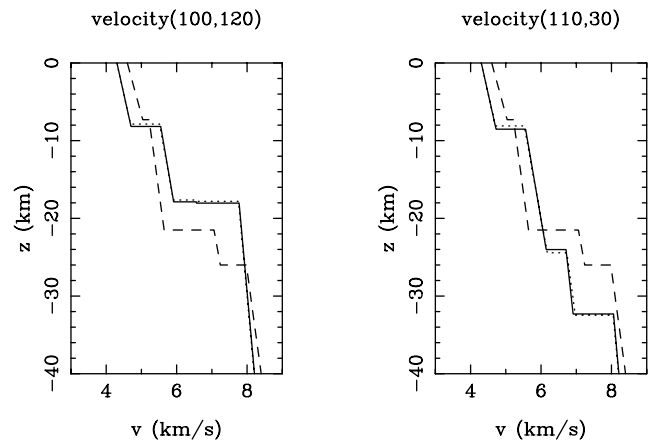The next step in the inversion process is to specify the model parametrization. The model must have the capacity (i.e. sufficient model parameters) to satisfy the data constraints adequately. By studying all of the available refraction sections, we were able to identify three crustal refraction phases and, usually, their associated reflection phases, as well as a P_n phase and a P_mP phase (Table 3). Strong P_mP phases are a feature common to all the refraction sections, suggesting a significant velocity contrast between lower crust and lithospheric mantle. The phases identified from the refraction sections indicate that the region of interest is best represented by three crustal layers overlying a mantle half-space. We obtained an approximate picture of the crustal structure by 1-D inversion of reflection and refraction traveltimes from the station/shot-line combinations 10/5, 31/5, 31/8 and 27/9 (each considered separately). These analyses provided depth to interface, layer velocity and layer velocity gradient. The average (1-D) structure determined from these 1-D inversions was used as the initial model estimate in the 3-D inversion. The diagonal entries of the *a priori* model covariance matrix are given by the variance of these interface depths, layer velocities and layer velocity gradients.

For the 3-D inversion, the upper and middle interfaces are each described by 63 nodes with variable spacing and the bottom interface by 120 nodes on a regular grid (Fig. 12). We reduced the node density in the upper two interfaces because the restricted geometry of the source–receiver array (Fig. 11) means that these interfaces, which occur at shallow depths, include large regions that are not intersected by any rays (see Fig. 15b). We invert for a total of 254 parameters (246 interface, four velocity and four velocity gradient). The source and receiver locations (Fig. 11) are projected into Cartesian space using an Albers equal-area conic projection with two standard parallels. On this scale, corrections for the Earth's sphericity are not necessary (Zelt 1999).

Ray tracing through the model is performed with all shot points at sea level ($z = 0$) and all receivers at their measured heights above sea level; station 39 has the greatest elevation at 975 m. In the inversion, the dimension of the subspace was set to 18. As in the synthetic data inversion (Section 3), 10 vectors lie in interface depth parameter space, four span velocity parameter space and four span velocity gradient parameter space, resulting in a scheme that offers an acceptable compromise
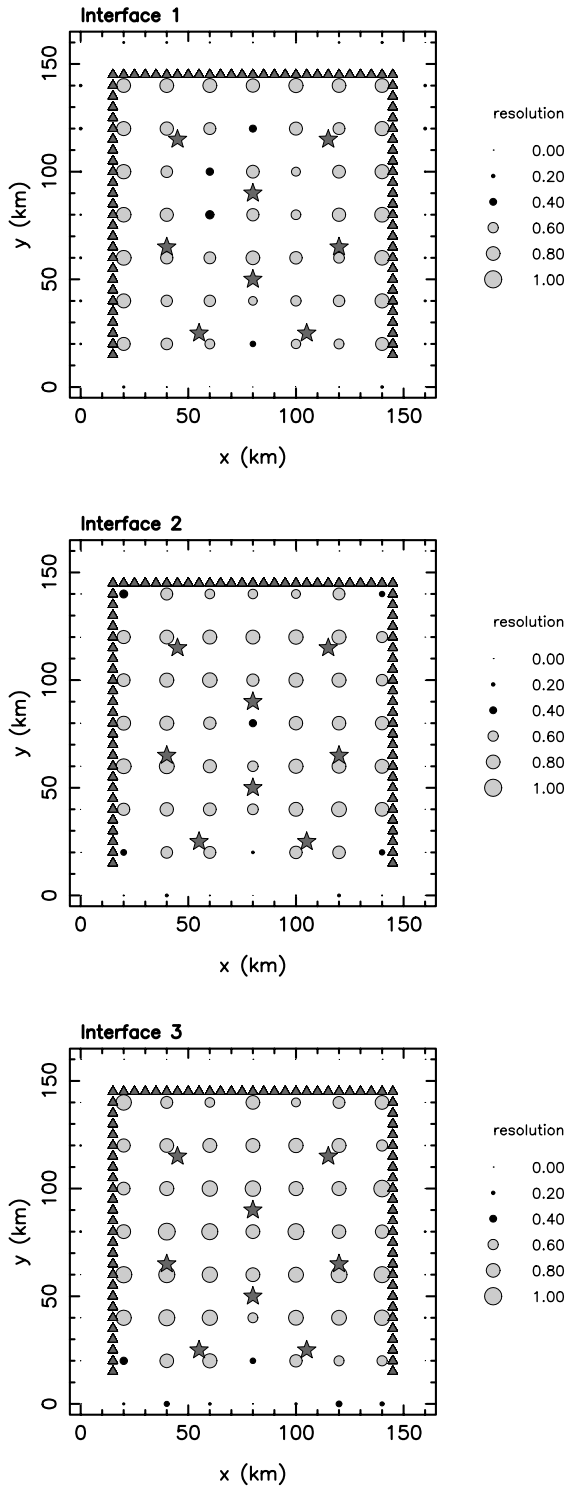
Figure 9. Graphical representation of the diagonal elements of the resolution matrix (calculated after six iterations of the method) for all interface depth parameters. The circles that indicate the size of the resolution are grey-filled for values ≥0.5 and black-filled for values <0.5.
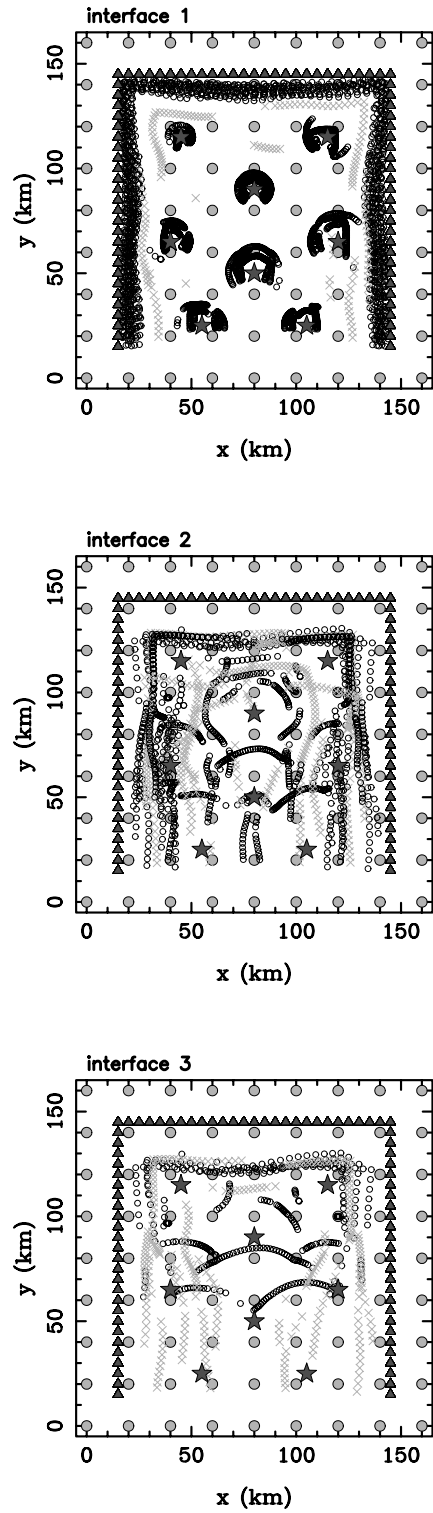

Figure 10. Ray–interface hits for synthetic test solution model (Fig. 6). Interface nodes are denoted by grey-filled circles, sources by stars and receivers by triangles. Rays that transmit through an interface are denoted by black circles and rays that reflect are denoted by grey crosses.

between the magnitude of the objective function reduction per iteration and computational effort. The value of the damping parameter ε was set to 1.0 on the basis of the trade-off between χ^2 misfit and rms model perturbation as ε is varied from 0 to 100 (Fig. 13a). A plot of χ^2 misfit versus iteration (Fig. 13b) for

$\varepsilon = 1.0$ follows a monotonically decreasing path that levels out close to the optimum value of 1.0 ($\chi^2 = 1.1$ at iteration 5). The corresponding rms data misfit at iteration 5 is 116 ms, which is 1 ms greater than the rms picking error.

Table 3. Phases picked from the available data. P_1P, P_2P and P_mP phases reflect off the top, middle and bottom interfaces respectively. P, P_1 and P_2 phases refract or turn back to the surface in the top, middle and bottom crustal layers respectively while the P_n phase enters the mantle half-space before refracting back to the surface. Superscripts indicate the number of picks associated with each phase of the indicated station–line combination.

Station	Line 5		Line 8		Line 9	
	refract	reflect	refract	reflect	refract	reflect
4						P_mP^{25}
5			P_2^{27}	P_mP^{28}		P_2^{19}
10	P^{12}, P_1^{45} P_2^{41}, P_n^{30}	P_2P^{21}, P_mP^{61}				
25		P_mP^{16}		P_mP^{28}		
27	P_2^{42}, P_n^{28}	P_mP^{63}	P_n^{36}		P_2^{38}, P_n^{41}	P_mP^{55}
31	P^{12}, P_1^{17} P_2^{25}, P_n^{23}	P_1P^{12}, P_2P^{18} P_mP^{54}	P_1^{26}, P_2^{25}	P_2P^{19}, P_mP^{28}	P_n^{33}	P_mP^{46}
39	P_2^{23}, P_n^{11}	P_mP^{44}			P_1^{21}, P_2^{9}	P_mP^{38}
40	P^{9}, P_1^{33} P_2^{23}, P_n^{18}	P_1P^{8}, P_2P^{19} P_mP^{43}			P_n^{13}	P_mP^{39}

Data recorded at station 10 from line 5 shots are shown in the wide-angle section of Fig. 14(a), and Fig. 14(b) shows a comparison between the picked and model traveltimes of both refracted and reflected phases from this section. The model traveltimes are generally within picking error, although some of the shorter-wavelength features evident in the observed data are not present in the model traveltime curves.

Fig. 15(a) shows the final model interface depth maps after five iterations with $\varepsilon = 1.0$. Ray interface intersection points are shown in Fig. 15(b) and the diagonal elements of the resolution matrix for the interface node depths (determined at the final solution) are shown in Fig. 15(c). Three cross-sections of constant x through the initial and solution models are shown in Fig. 16. From the ray hit (Fig. 15b) and resolution (Fig. 15c)
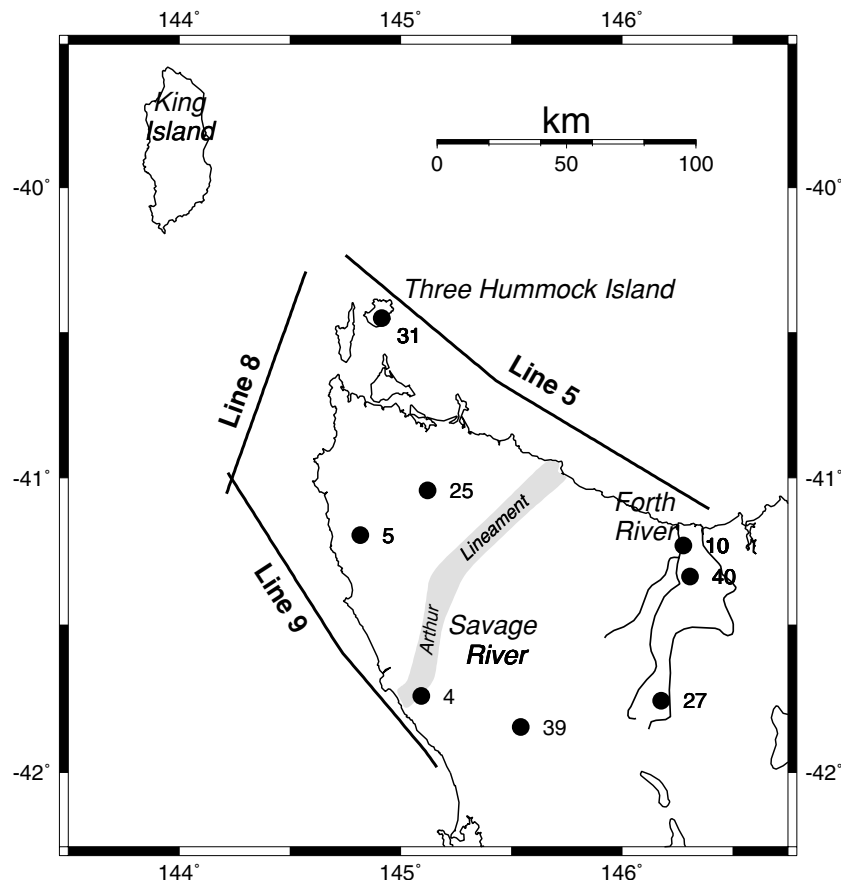

Figure 11. Subset of TASGO source–receiver array in NW Tasmania used in the inversion for crustal structure. Black dots indicate recorders and thick solid lines indicate shot lines (50 m shot spacing).
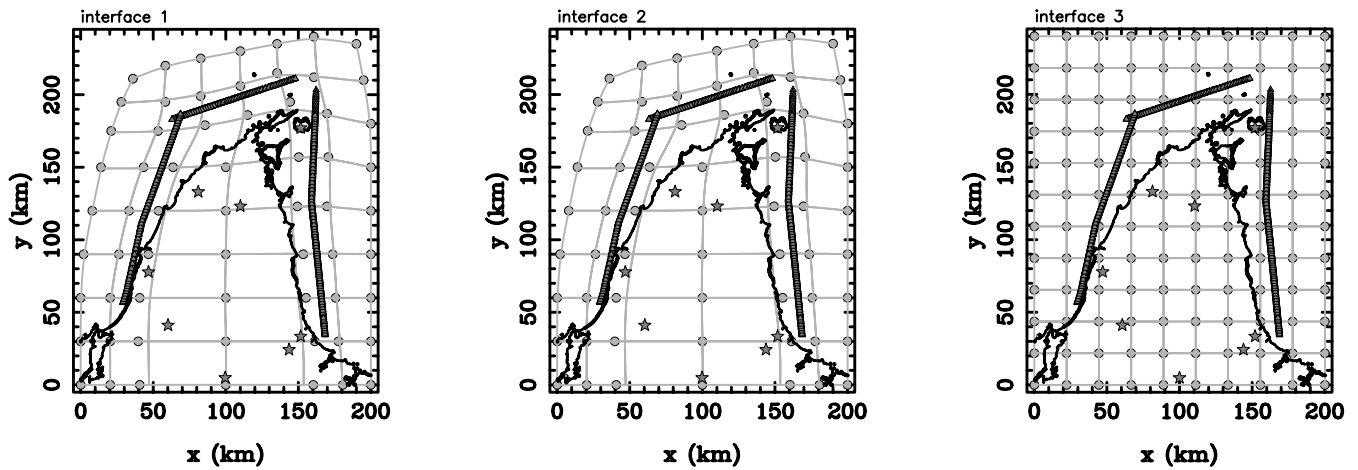
Figure 12. Horizontal node distribution used for each of the three interfaces (numbered in order of increasing depth). Sources and receivers are indicated by triangles and stars respectively, while interface vertices are denoted by grey-filled circles. Grey lines represent surface patch boundaries.
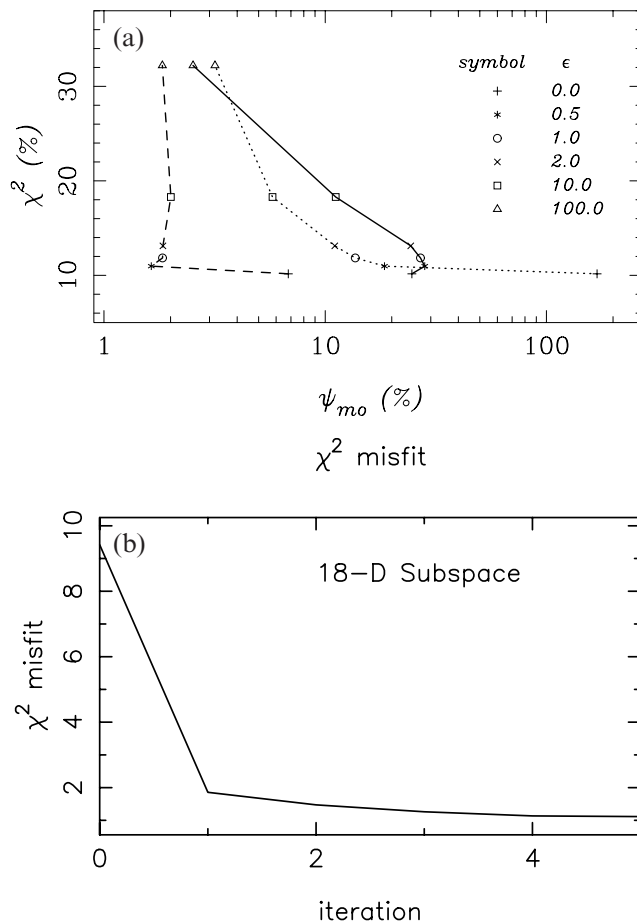

Figure 13. (a) χ^2 data misfit (eq. 17) versus rms model perturbation ψ_{mo} (eq. 18) for various values of the damping factor ε after five iterations. The two misfit measures χ^2 and ψ_{mo} are plotted as a percentage of their initial values (i.e. at iteration zero). The model perturbation ψ_{mo} is determined separately for each parameter type: interface node depth (solid line), layer velocity (dashed line) and layer velocity gradient (dotted line). (b) χ^2 misfit versus iteration number for the inversion solution shown in Fig. 15 with $\varepsilon = 1.0$.

diagrams, it is evident that the top interface is very poorly constrained by the data; most of the ray hit marks coincide with the source and receiver symbols. The large offset relative to interface depth means that reflections are difficult to detect. In this inversion method, regions that are poorly resolved tend not to deviate significantly from their initial value and are unlikely to influence the reconstruction of deeper structure strongly. Although interface 1 is poorly resolved, its presence in the model parametrization does not adversely effect the resolution of the other interface and velocity parameters. The deflections from the horizontal of interface 1 are of small amplitude (Fig. 16) and do not affect the traveltimes of deeper phases enough to have any significant effect on the depths of deeper interfaces. We verified this assertion by running the inversion with the upper interface nodes forced to remain at their initial depths. The bottom two interfaces were then practically identical to the corresponding interfaces derived without this constraint, although the overall data fit was not quite as good. Based on the interpretation of the resolution parameters (Fig. 15c), the major depth anomalies of interface 2 are resolved near the shot lines, although not inland. The bottom interface, which represents the Moho, is by far the best resolved interface (Fig. 15c), mainly because of the profusion of $P_{\mathrm{m}}P$ phases (Fig. 15b) picked from the data.

A comparison of the initial and final layer velocity structures are given by the three velocity versus depth curves in Fig. 17. The layer velocities (Tables 4 and 5) have not changed greatly from their initial estimates, but we found that if we fix the velocity estimates and invert for interface structure alone, the final rms data misfit is 76 ms greater than the result we obtained by inverting for all three parameter classes. Table 4 also shows the resolution of each of the velocity parameters. Generally, velocity (v_{o}) is well resolved but velocity gradient (k) is not, especially in the top two layers. The poor resolution of k is expected because both layers are relatively thin and rays that turn in these layers are few in number. The average crustal velocity (all three layers) of the final model is 6.3 km s^{-1} and the average velocity of the mantle immediately below the Moho is 8.2 km s^{-1}.

Table 4. Velocity parameter values of initial and final models for the NW Tasmania data set. The resolution values associated with the recovered model are also given. Layer 1 is the upper crustal (top) layer and layer 4 is the mantle half-space. Note that the actual velocity at a given depth is defined by eq. (1).

Layer	Initial model		Recovered model		Resolution	
	v_0 (km s^{-1})	k (s^{-1})	v_0 (km s^{-1})	k (s^{-1})	v_0	k
1	4.90	0.045	4.92	0.044	0.98	0.002
2	5.50	0.037	5.65	0.031	0.98	0.090
3	6.00	0.035	5.98	0.029	0.98	0.520
4	7.00	0.027	7.17	0.031	0.68	0.347

Table 5. Average velocities (in km s^{-1}) immediately above (v_A^a) and below (v_A^b) the initial and recovered model interfaces for the TASGO data inversion.

Interface	Initial model		Recovered model	
	v_A^a	v_A^b	v_A^a	v_A^b
1	4.98	5.57	4.98	5.70
2	5.78	6.26	5.90	6.21
3	7.12	7.86	6.90	8.16

5 DISCUSSION

In the analysis of 2-D wide-angle seismic data sets, crustal structure is commonly represented by a series of layers of variable thickness. Interfaces are usually defined by piecewise polynomials (of degree one or higher) and the velocity parametrization of each layer often allows for lateral variation. During the reconstruction process, both parameter types (interface depth and velocity) are usually varied in an attempt to satisfy the data, which normally consist of the traveltimes of both refracted and reflected phases. For example, Stadtlander *et al.* (1999) derived a crustal and upper mantle structure beneath the southern Ural Mountains, representing upper, middle and lower crustal layers in addition to an upper mantle half-space. They also divided the upper crust into a large number of laterally discontinuous layers. Kodaira *et al.* (1998) used wide-angle

traveltimes to constrain a crustal model consisting of no fewer than eight layers, four of which were laterally discontinuous, beneath the Jan Mayan microcontinent. They inverted for both interface geometry and layer velocity structure. Others who have used similar approaches to constrain 2-D multilayered crustal structure include Kanasewich *et al.* (1994), Darbyshire *et al.* (1998), Navin *et al.* (1998) and Vogt *et al.* (1998).

Dealing with complex multiple interface structures with variable velocity layers is more problematic in three dimensions than in two. Thus, although a number of tomographic-style interpretations of 3-D wide-angle data have been performed, most authors avoid the kind of detail seen in the class of 2-D models described above. For example, it is common practice to invert the traveltimes of only the first arrivals of a 3-D data set for continuous velocity structure (e.g. Hole 1992; Zelt & Barton 1998) or to invert for the structure of a single interface using first arrivals (e.g. Hole *et al.* 1992) or reflected phases (e.g. Riahi *et al.* 1997). In 3-D problems, a dense coverage of rays is much more difficult to achieve than in two dimensions, even if both
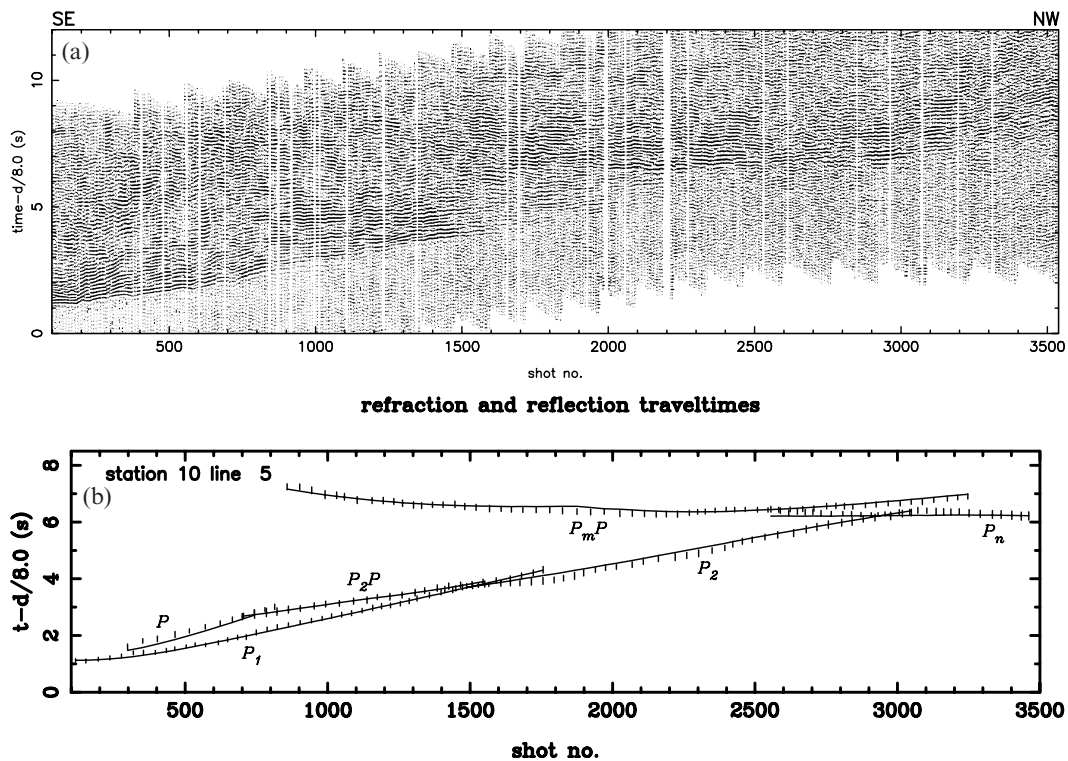

Figure 14. (a) Wide-angle data collected at station 10 from line 5 shots (see Fig. 11). Bandpass filtering between 4.0 and 14.0 Hz and nine-trace stacking have been employed to improve signal:noise ratio. (b) Comparison between observed picks (error bars) from (a) and solution model traveltimes (solid lines) of refracted and reflected phases.
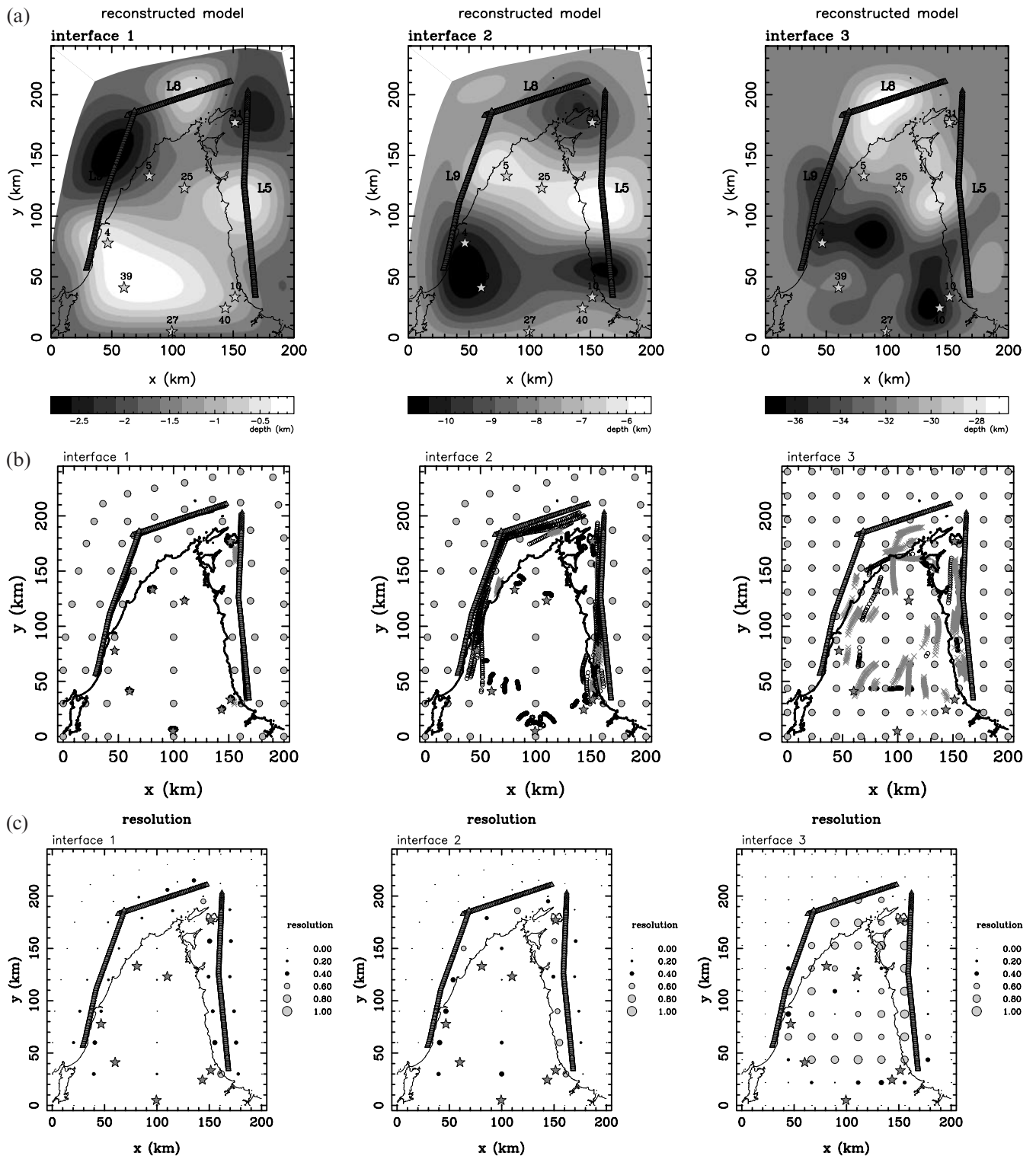
Figure 15. (a) Interface depth maps for NW Tasmania after five iterations. The top two interfaces are non-rectangular due to the irregular parametrization (Fig. 12). (b) Ray–interface hits for this model. Rays that cross an interface are denoted by black circles and rays that reflect are denoted by grey crosses. (c) Diagonal elements of the resolution matrix. Circles are grey-filled for values ≥0.5 and black-filled for values <0.5. Receivers are denoted by stars and sources by triangles in all three plots.

refraction and wide-angle reflection data are used. Zelt *et al.* (1996) used a layer-stripping approach to invert refraction and reflection traveltimes for interface structure and layer velocity beneath the southwestern Canadian Cordillera. The method we have presented here is designed to invert both refraction and reflection traveltimes for crustal structure in the form of multiple laterally continuous interfaces separating subhorizontal layers that are free to pinch out. Thus, our inversion method has
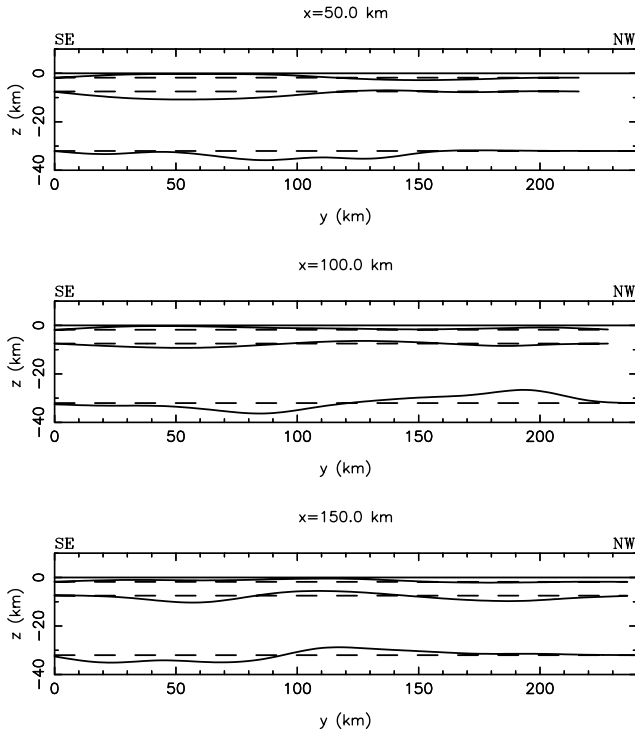
Figure 16. Three cross-sections taken at constant *x* through the reconstructed model (solid lines) after five iterations and the initial model (dashed lines) of NW Tasmania. Refer to Table 4 for layer velocities and Fig. 15(a) for cross-section locations.

many similarities with those methods commonly used in 2-D analyses. Perhaps the main difference is that our parametrization does not include lateral velocity variations within a layer. However, 3-D data sets such as the TASGO data set may not provide adequate ray coverage to allow for the satisfactory resolution of both lateral velocity variation and interface structure, even allowing for the use of both refraction and reflection phases. Our approach has been to look for the simplest model capable of explaining the data. If a model without lateral velocity variation is capable of satisfying the available data within observational error, then there is little to justify the inclusion of more model parameters, which will only produce a more complex solution.

The interface parametrization based on cubic B-splines (eq. 2) is quite general in that interface vertices are not restricted to a

rectangular grid and the interface itself need not be a single-valued function with respect to depth. A non-rectangular grid of nodes may be useful if ray coverage is highly variable, as demonstrated in Section 4 with the TASGO data example. The ray tracing method (Section 2.2) is designed to deal with interfaces that are not single valued with respect to depth, but it would be difficult to identify phases picked from a refraction section with recumbent structures.

The synthetic tests (Section 3) show that the method is capable of simultaneously inverting refraction and reflection traveltimes for interface structure and linear velocity variations with depth within layers. The method is robust in the presence of Gaussian-distributed data noise, a source–receiver configuration (Fig. 2) that is far from homogeneous, and initial model estimates that are not close to the true model (see Table 2 and Fig. 7). The synthetic model (Fig. 6) includes a layer pinch-out, and the inversion demonstrates that these structures may be derived from wide-angle data even if an initial model with only 1-D structure is used. The initial model used in Section 3 has an rms traveltime misfit of 624 ms, which is reduced to 76 ms after six iterations. The simultaneous inversion of all data for all model parameters means that, contrary to the layer stripping approach, each model parameter in the inversion process is influenced by all of the ray paths that are affected by that parameter. Although not described in the synthetic tests, low-velocity layers and layers with negative velocity gradients significantly reduce the number of turning rays, which will generally result in poorly constrained velocity parameters within the layer.

The results of the TASGO data inversion demonstrate that the method is capable of producing a solution that satisfies real data. Undesirable aspects of the data set include large regions with poor data coverage and a relative lack of rays that reflect or refract back towards the surface from the upper two interfaces. These properties of the data set are revealed in the ray coverage (Fig. 15b) and model resolution (Fig. 15c) plots, which indicate that large areas of the upper crustal interfaces are not resolved by the data. The interface that represents the Moho is, on the other hand, generally well resolved by the data, and tests indicate that the lack of resolution in the upper interfaces is unlikely to affect the accuracy of the Moho reconstruction.

The TASGO wide-angle data set was collected concurrently with normal-incidence reflection data. In principle, traveltime picks from the normal-incidence component of the survey
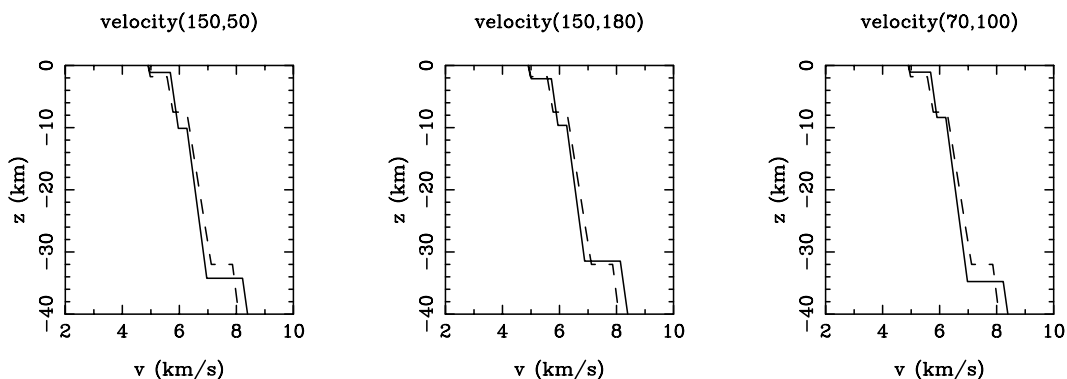

Figure 17. Velocity versus depth at three locations (see Fig. 15a) in the reconstructed model of NW Tasmania. Dashed lines denote the initial model and solid lines denote the final model after five iterations.

could have been used in the inversion, but this would have required significant additional effort, and while they would provide extra control beneath the shot lines, they would not help constrain structure beneath the onshore region bounded by the shot-line array where resolution is poorest, especially of interfaces 1 and 2.

According to Brown *et al.* (1998), Tasmania consists of seven Proterozoic–early Palaeozoic fault-bounded tectonic elements overlain by much younger late Palaeozoic–early Mesozoic and Cenozoic cover. The region of NW Tasmania that we have modelled is predominantly overlain by clastic carbonate and metasedimentary units that are approximately 2 km thick (Williams 1989). This sequence is represented in our model (Fig. 16) by the thin overlying layer that varies in thickness between 0.2 and 2.6 km. Inspection of the multichannel reflection sections also shows a thin upper layer, below which lies a thicker layer that extends to approximately 7 km depth. The reflection seismic signature of this second layer has been interpreted (Barton 1999) as a series of adjacent granitoid bodies and Neoproterozoic volcanics. Our 3-D model represents this zone as a continuous layer whose lower interface varies in depth between 5.5 and 11 km. Interestingly, the region where the base of this layer (interface 2) shallows (Fig. 15a: $x = 160$ km, $y = 110$ km) corresponds to the thinner volcanics and where it is deeper (Fig. 15a: $x = 160$ km, $y = 50$ km) corresponds to a deeper-rooted granite body seen in the reflection section interpreted by Barton (1999). The lower crustal layer (third layer) in our model is as much as 30 km thick in some places. In the reflection section, the corresponding depth range is largely devoid of any coherent reflections, which suggests that there are no other important interfaces within this layer. The variations in depth of the Moho interpreted from the reflection section along line 5 (Barton 1999) are also consistent with depth variations derived here from inversion of the wide-angle data. The resolved portions of the Moho indicate a general thickening of the crust from the NW to the SE, in broad agreement with the surface elevation, which increases towards the centre of the island.

One of the more significant surface features in NW Tasmania is the Arthur Lineament (Fig. 11), an approximately 10 km wide belt of strongly deformed, metamorphosed rocks that trends NE–SW. Little is known about the depth extent and origin of this structure, although Corbett (1994) has suggested that it may be a leading-edge effect of deformation caused by an orogenic event prior to the Cambrian. The upward deflection of the lower crustal layer seen in our model on the $x = 150$ km profile (Fig. 16) between $y = 80$ km and $y = 120$ km lies approximately beneath the Arthur Lineament.

6   CONCLUSIONS

We have described a new method for the determination of 3-D crustal structure by simultaneous inversion of seismic refraction and wide-angle reflection traveltimes for both interface geometry and layer velocity. The cubic B-spline parametrization used to describe interface structure permits a wide variety of geometries to be represented, and the assumption that velocity varies linearly with depth in each layer allows for analytic expression of the ray paths and a relatively small number of model parameters. The forward problem of determining the traveltime and ray path of a specified phase between source and receiver is solved using a shooting method that proves to be

robust even in the presence of complex structures. The inverse problem is solved using a subspace inversion method that is efficient and allows multiple parameter classes (interface depths, layer velocities and layer velocity gradients) to be inverted simultaneously without the need for arbitrary weighting methods. Synthetic tests show that the method can produce accurate reconstructions of multi-interface models despite data noise, relatively inaccurate initial models and an irregular source–receiver configuration. These tests also show that estimates of resolution taken at the solution point and based on linear theory are a useful tool in assessing the robustness of the reconstructed model. Application of the method to a subset of the TASGO wide-angle data set produced a three-layer crustal model that is consistent with known surface geology and independent interpretations of normal-incidence reflection data, yet provides new information about crustal thickness variations beneath Tasmania. Moho depth beneath NW Tasmania varies from about 27 to 37 km, with the major change in depth occurring across the Arthur Lineament.

REFERENCES

Barsky, B.A., 1982. End conditions and boundary conditions for uniform B-spline curve and surface representations, *Computers in Industry,* **3,** 17–29.

Bartels, R.H., Beatty, J.C. & Barsky, B.A., 1987. *An Introduction to Splines for Use in Computer Graphics and Geometric Modelling,* Morgan Kaufmann, Los Altos.

Barton, T.J., 1999. Crustal structure of northern Tasmania based upon a deep seismic transect, in *Last Conference of the Millenium,* Vol. 53, 3–4, Geological Society of Australia, Sydney.

Bishop, T.P., *et al.*, 1985. Tomographic determination of velocity and depth in laterally varying media, *Geophysics,* **50,** 903–923.

Brown, A.V., Seymour, D.B., Calver, C.R., Green, G.R. & Yeates, A.N., 1998. Overview of Tasmania's tectonic framework, geological history and mineralisation, in *Mineral Systems and the Crust–Upper Mantle of Southeast Australia, Record 1998/2,* 13–24, Australian Geological Survey Organisation, Canberra.

Carroll, S. & Beresford, G., 1996. Combining reflection tomography with layer replacement for velocity analysis of near-surface reefs, *Geophysics,* **61,** 561–569.

Cheng, N. & House, L., 1996. Minimum traveltime calculations in 3-D graph theory, *Geophysics,* **61,** 1895–1898.

Chiarabba, C., Amoto, A. & Meghraoui, M., 1997. Tomographic images of the El Asnam fault zone, *J. geophys. Res.,* **102,** 24 485–24 498.

Chiu, S.K.L., Kanasewich, E.R. & Phadke, S., 1986. Three-dimensional determination of structure and velocity by seismic tomography, *Geophysics,* **51,** 1559–1571.

Chudyk, E.C., Bracewell, R. & Collins, C.D.N., 1995. *Operational Report for the 1995 Seismic Refraction, Wide-Angle Reflection and Tomography Survey of Tasmania,* Record 1995/74, Australian Geological Survey Organisation, Canberra.

Corbett, K., 1994. Stratigraphic mapping, Tyennan connection, Cambrian orogenies, the Arthur Lineament, and the tectonic context of the Mount Read Volcanics, in *Abstracts,* Vol. 39, 35–37, Geological Society of Australia, Sydney.

Darbyshire, F.A., Bjarnason, I.J., White, R.S. & Flórenz, O.G., 1998. Crustal structure above the Iceland mantle plume imaged by the ICEMELT refraction profile, *Geophys. J. Int.,* **135,** 1131–1149.

Farra, V. & Madriaga, R., 1988. Non-linear reflection tomography, *Geophys. J.,* **95,** 135–147.

Hill, P.J. & Yeates, A.N., 1995. *Circum-Tasmania and South Tasman Rise: Cruise Proposal for Deep Crustal Seismic Data Acquisition,* Record 1995/13, Australian Geological Survey Organisation, Canberra.

Hole, J.A., 1992. Nonlinear high-resolution three-dimensional travel-time tomography, *J. geophys. Res.,* **97,** 6553–6562.

Hole, J.A., Clowes, R.M. & Ellis, R.M., 1992. Interface inversion using broadside seismic refraction data and three-dimensional traveltime calculations, *J. geophys. Res.,* **97,** 3417–3429.

Julian, B.R. & Gubbins, D., 1977. Three-dimensional seismic ray tracing, *J. Geophys.,* **43,** 95–113.

Kanasewich, E., *et al.,* 1994. Crustal velocity structure of the Omineca Belt, southwestern Canadian Cordillera, *J. geophys. Res.,* **99,** 2653–2670.

Kennett, B.L.N., Sambridge, M.S. & Williamson, P.R., 1988. Subspace methods for large scale inverse problems involving multiple para-meter classes, *Geophys. J.,* **94,** 237–247.

Kodaira, S., Mjelde, R., Gunnarsson, K., Shiobara, H. & Shimamura, H., 1998. Structure of the Jan Mayen micro-continent and implications for its evolution, *Geophys. J. Int.,* **132,** 383–400.

Lévêque, J.J., Rivern, L. & Wittlinger, G., 1993. On the use of the checker-board test to assess the resolution of tomographic inversions, *Geophys. J. Int.,* **115,** 313–318.

Lutter, W.J. & Nowack, R.L., 1990. Inversion for crustal structure using reflections from the PASSCAL Ouachita experiment, *J. geophys. Res.,* **95,** 4633–4646.

Lutter, W.J., Nowack, R.L. & Braile, L., 1990. Seismic imaging of upper crustal structure using travel times from the PASSCAL Ouachita experiment, *J. geophys. Res.,* **95,** 4621–4631.

McCaughey, M. & Singh, S.C., 1997. Simultaneous velocity and interface tomography of normal-incidence and wide-aperture seismic traveltime data, *Geophys. J. Int.,* **131,** 87–99.

Navin, D.A., Peirce, C. & Sinha, M.C., 1998. The RAMESSES experiment—II. Evidence for accumulated melt beneath a slow spreading ridge from wide-angle refraction and multichannel reflection seismic profiles, *Geophys. J. Int.,* **135,** 746–772.

Nowack, R.L. & Lyslo, J.A., 1989. Fréchet derivatives for curved interfaces in the ray approximation, *Geophys. J.,* **97,** 497–509.

Riahi, M.A., Lund, C.E. & Pederson, L.B., 1997. Three-dimensional image of the Moho undulations beneath the Gulf of Bothnia using wide-angle seismic data, *Geophys. J. Int.,* **129,** 461–471.

Sambridge, M.S., 1990. Non-linear arrival time inversion: constraining velocity anomalies by seeking smooth models in 3-D, *Geophys. J. Int.,* **102,** 653–677.

Sambridge, M.S. & Kennett, B.L.N., 1990. Boundary value ray tracing in a heterogeneous medium: a simple and versatile algorithm, *Geophys. J. Int.,* **101,** 157–168.

Sethian, J.A. & Popovici, A.M., 1999. 3-D traveltime computation using the fast marching method, *Geophysics,* **64,** 516–523.

Shalev, E., 1993. Cubic B-slines: strategies of translating a simple structure to B-spline paramterization, *Bull. seism. Soc. Am.,* **83,** 1617–1627.

Stadtlander, R., Mechie, J. & Schulze, A., 1999. Deep structure of the southern Ural mountains as derived from wide-angle seismic data, *Geophys. J. Int.,* **137,** 501–515.

Steck, L.K., Thurber, C.H., Fehler, M., Lutter, W.J., Roberts, P.M., Baldridge, W.S., Stafford, D.G. & Sessions, R., 1998. Crust and upper mantle *P* wave velocity structure beneath Valles caldera, New Mexico: results from the Jemez teleseismic tomography experiment, *J. geophys. Res.,* **103,** 24 301–24 320.

Tarantola, A., 1987. *Inverse Problem Theory,* Elsevier, Amsterdam.

Telford, W.M., Geldart, L.P., Sheriff, R.E. & Keys, D.A., 1976. *Applied Geophysics,* Cambridge University Press, Cambridge.

Vidale, J.E., 1990. Finite-difference calculations of traveltimes in three dimensions, *Geophysics,* **55,** 521–526.

Vogt, U., Makris, J., O'Reilly, B., Hausser, F., Readman, P.W., Jacob, A.W.B. & Shannon, P.M., 1998. The Hatton Basin and continental margin: crustal structure from wide-angle seismic and gravity data, *J. geophys. Res.,* **103,** 12 545–12 566.

Wang, B. & Braile, L.W., 1996. Simultaneous inversion of reflection and refraction seismic data and application to field data from the northern Rio Grande rift, *Geophys. J. Int.,* **125,** 443–458.

White, D.J., 1989. Two-dimensional seismic refraction tomography, *Geophys. J.,* **97,** 223–245.

Williams, E., 1989. Summary and synthesis, in *Geology and Mineral Resources of Tasmania,* Spec. Publ., Vol. 15, 468–499, eds Burrett, C.F. & Martin, E.L., Geological Society of Australia, Sydney.

Williamson, P.R., 1990. Tomographic inversion in reflection seismology, *Geophys. J. Int.,* **100,** 255–274.

Zelt, B.C., Ellis, R.M., Clowes, R.M. & Hole, J.A., 1996. Inversion of three-dimensional wide-angle seimic data from the southwestern Canadia Cordillera, *J. geophys. Res.,* **286,** 209–221.

Zelt, C.A., 1994. 3-D velocity structure from simultaneous traveltime inversion of in-line seismic data along intersecting profiles, *Geophys. J. Int.,* **118,** 795–801.

Zelt, C.A., 1999. Modelling strategies and model assessment for wide-angle seismic traveltime data, *Geophys. J. Int.,* **139,** 183–204.

Zelt, C.A. & Barton, P.J., 1998. Three-dimensional seismic refraction tomography: a comparison of two methods applied to data from the Faeroe Basin, *J. geophys. Res.,* **103,** 7187–7210.

Zelt, C.A. & Smith, R.B., 1992. Seismic traveltime inversion for 2-D crustal velocity structure, *Geophys. J. Int.,* **108,** 16–34.

Zelt, C.A. & Zelt, B.C., 1998. Study of out-of-plane effects in the inversion of refraction/wide-angle reflection traveltimes, *Tectonophysics,* **286,** 209–221.

Zelt, C.A., Hojka, A.M., Flueh, E.R. & McIntosh, K.D., 1999. 3D simultaneous seismic refraction and reflection tomography of wide-angle data from the central Chilean margin, *Geophys. Res. Lett.,* **26,** 2577–2580.

APPENDIX A FRÉCHET DERIVATIVES

A1 Fréchet derivatives for velocity and velocity gradient

Fréchet derivatives for velocity parameters are usually derived by assuming that a velocity perturbation does not cause a perturbation of the ray path, resulting in first-order accurate expressions according to Fermat's principle (e.g. White 1989). We derive analytic expressions for the Fréchet derivatives assuming only that the endpoints of ray segments are fixed. Where this assumption is valid, exact analytic expressions for the Fréchet derivatives are obtained (e.g. for rays that do not interact with any interface). Where interfaces are involved, the resulting expressions provide accurate approximations. The basic problem, to find the derivatives $\partial t/\partial v_0$ and $\partial t/\partial k$ for a ray between two points in a layer, can be considered in two dimensions since all ray path segments must lie in a vertical plane. In the following derivations, notation is consistent with that used in the main body of the paper.

Consider a ray path segment that originates at (x_o, z_o) and ends at (x_e, z_e) with the *x*-axis defined such that $x_e > x_o$. The ray path between the two points is given parametrically by

$$x_e = \frac{v(z_o)}{k}\left[\frac{(c_e - c_o)}{\sqrt{1 - c_o{}^2}}\right] + x_o, \tag{A1}$$

$$z_e = \frac{v(z_o)}{k}\left[1 - \sqrt{\frac{1 - c_e{}^2}{1 - c_o{}^2}}\right] + z_o, \tag{A2}$$

and the traveltime is

$$t = \frac{1}{2k} \ln\left[\left(\frac{1+c_e}{1-c_e}\right)\left(\frac{1-c_o}{1+c_o}\right)\right], \tag{A3}$$

where c_o and c_e are the vertical components of the unit tangent vector to the ray segment at (x_o, z_o) and (x_e, z_e) respectively. The partial derivative of traveltime with respect to the velocity parameter v_0 is

$$\frac{\partial t}{\partial v_0} = \frac{\partial t}{\partial c_o}\frac{\partial c_o}{\partial v_0} + \frac{\partial t}{\partial c_e}\frac{\partial c_e}{\partial v_0}. \tag{A4}$$

$\partial t/\partial c_o$ and $\partial t/\partial c_e$ are easily calculated from eq. (A3) as

$$\frac{\partial t}{\partial c_o} = \frac{1}{k(c_o^2 - 1)} \quad \text{and} \quad \frac{\partial t}{\partial c_e} = \frac{1}{k(1 - c_e^2)}. \tag{A5}$$

To obtain $\partial c_o/\partial v_0$ and $\partial c_e/\partial v_0$, we rearrange eqs (A1) and (A2) to obtain, respectively,

$$c_e = c_o + r\sqrt{1 - c_o^2} \quad \text{and} \quad 1 - c_e^2 = s^2(1 - c_o^2), \tag{A6}$$

where $r = k(x_e - x_o)/(v_0 - kz_o)$ and $s = 1 - k(z_e - z_o)/(v_0 - kz_o)$. Implicit differentiation of each expression in eq. (A6) with respect to v_0 and solving the resulting system of two linear equations for the two unknowns $\partial c_o/\partial v_0$ and $\partial c_e/\partial v_0$ yields

$$\frac{\partial c_o}{\partial v_0} = \frac{k(1 - c_o^2)[c_e(x_o - x_e) - s(z_o - z_e)\sqrt{1 - c_o^2}]}{v(z_o)^2[rc_e c_o + (c_o s^2 - c_e)\sqrt{1 - c_o^2}]}, \tag{A7}$$

$$\frac{\partial c_e}{\partial v_0} = \frac{sk(1 - c_o^2)[c_o s(x_o - x_e) + (z_o - z_e)(rc_o - \sqrt{1 - c_o^2})]}{v(z_o)^2[rc_e c_o + (c_o s^2 - c_e)\sqrt{1 - c_o^2}]}. \tag{A8}$$

The partial derivative of traveltime with respect to the velocity gradient parameter k is

$$\frac{\partial t}{\partial k} = \frac{\partial t}{\partial c_o}\frac{\partial c_o}{\partial k} + \frac{\partial t}{\partial c_e}\frac{\partial c_e}{\partial k} - \frac{1}{2k^2}\ln\left[\left(\frac{1+c_e}{1-c_e}\right)\left(\frac{1-c_o}{1+c_o}\right)\right], \tag{A9}$$

where the third term on the right-hand side is included since k appears explicitly in eq. (A3). The partial derivatives $\partial c_o/\partial k$ and $\partial c_e/\partial k$ can be determined using the approach we employed to calculate $\partial c_o/\partial v_0$ and $\partial c_e/\partial v_0$, which gives

$$\frac{\partial c_o}{\partial k} = \frac{v_0(1 - c_o^2)[c_e(x_e - x_o) + s(z_o - z_e)\sqrt{1 - c_o^2}]}{v(z_o)^2[rc_e c_o + (c_o s^2 - c_e)\sqrt{1 - c_o^2}]}, \tag{A10}$$

$$\frac{\partial c_e}{\partial k} = \frac{sv_0(1 - c_o^2)[c_o s(x_e - x_o) + (z_e - z_o)(rc_o - \sqrt{1 - c_o^2})]}{v(z_o)^2[rc_e c_o + (c_o s^2 - c_e)\sqrt{1 - c_o^2}]}. \tag{A11}$$

A2 Fréchet derivatives for interface depth

The shape of a single surface patch depends on 16 vertices, so a single ray–interface intersection will contribute 16 partial derivatives of the form $[\partial t/\partial z_v^{k,l}]$, where $k, l = 1, \ldots, 4$ and z_v refers to the z-coordinate of an interface vertex. Exact analytic expressions for the Fréchet derivatives are out of the question, but relatively simple analytic formulae that are accurate to first order can be obtained. The basic approach for doing this has
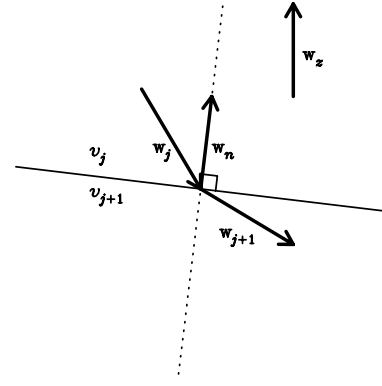

Figure A1. Notation for interface partial derivatives: $\mathbf{w}_n$ is a unit normal vector to the surface at the intersection point, $\mathbf{w}_j$ is a unit tangent vector to the ray in layer j that points towards the intersection point, $\mathbf{w}_{j+1}$ is a unit tangent vector to the ray in layer $j+1$ that points away from the intersection point and $\mathbf{w}_z = [0, 0, 1]$. v_j and v_{j+1} are the velocities in layers j and $j+1$ respectively.

been outlined by a number of authors (e.g. Nowack & Lyslo 1989; Sambridge 1990; Zelt & Smith 1992). Hence, we will only derive the component of the solution that is relevant to a uniform B-spline parametrization. As above, the notation used here is consistent with the main body of the paper.

The perturbation in traveltime caused by the perturbation of an interface node is calculated by partitioning the problem

$$\frac{\partial t}{\partial z_v^{k,l}} = \frac{dt}{dh_{int}}\frac{dh_{int}}{dz_{int}}\frac{\partial z_{int}}{\partial z_v^{k,l}}, \tag{A12}$$

where h_{int} is displacement normal to the interface at the point of intersection by the ray and z_{int} is the z-coordinate of the intersection point. Simple analytic formulae can be given for the two total derivatives in eq. (A12) if we assume that an interface perturbation does not result in a perturbation of the ray path. The aspect of eq. (A12) that is specific to B-splines is $\partial z_{int}/\partial z_v^{k,l}$, and given the form of eq. (2) it is simple to calculate

$$\frac{\partial z_{int}}{\partial z_v^{k,l}} = b_k(u_{int})b_l(v_{int}). \tag{A13}$$

Hence, the full expression is

$$\frac{\partial t}{\partial z_v^{k,l}} \approx \left[\frac{\mathbf{w}_j \cdot \mathbf{w}_n}{v_j} - \frac{\mathbf{w}_{j+1} \cdot \mathbf{w}_n}{v_{j+1}}\right][\mathbf{w}_n \cdot \mathbf{w}_z]b_k(u_{int})b_l(v_{int}), \tag{A14}$$

where v_j and v_{j+1} are respectively the velocity in the upper and lower layers at the intersection point, $\mathbf{w}_j$ and $\mathbf{w}_{j+1}$ are unit vectors parallel to the ray in layers j and $j+1$ respectively, $\mathbf{w}_z = [0, 0, 1]$ and $\mathbf{w}_n$ is a unit normal vector to the interface at the intersection point (see Fig. A1). $\mathbf{w}_j$ always points towards the interface and $\mathbf{w}_{j+1}$ always points away from the interface irrespective of whether the ray is upgoing or downgoing. For reflections, $\mathbf{w}_{j+1} \cdot \mathbf{w}_n = -\mathbf{w}_j \cdot \mathbf{w}_n$ and $v_{j+1} = v_j$ in eq. (A14).

All three classes of Fréchet derivative calculation defined in this Appendix have been tested by comparison with finite difference approximations obtained by shooting rays through a model, perturbing a model parameter and reshooting the rays. Several of these tests were performed and good agreement between the analytic and numerical solutions occurred in all cases.